Radio Observations of Ultra Luminous Infra Red Galaxies (ULIRGs)

A Thesis

submitted to

Indian Institute of Science Education and Research Pune

in partial fulfilment of the requirements for the

BS-MS Dual Degree Programme

by

Sowkhya Shanbhog

Indian Institute of Science Education and Research Pune

Dr. Homi Bhabha Road,

Pashan, Pune 411008, INDIA.

May, 2023

Supervisor: Prof Mousumi Das

© Sowkhya Shanbhog 2023

Certificate

This is to certify that this dissertation entitled **Radio Observations of Ultra Luminous Infra Red Galaxies (ULIRGs)** towards the partial fulfilment of the BS-MS dual degree programme at the Indian Institute of Science Education and Research, Pune represents study/work carried out by Sowkhya Shanbhog at the Indian Institute of Astrophysics, Bengaluru and Indian Institute of Science Education and Research, Pune under the supervision of Prof Mousumi Das, Associate Professor, Indian Institute of Astrophysics, during the academic year 2022-2023.

_____
Sowkhya Shanbhog

_____
Prof Mousumi Das

Committee:

Prof Mousumi Das

Prof Ramana Athreya

Declaration

I hereby declare that the matter embodied in the report entitled **Radio Observations of Ultra Luminous Infra Red Galaxies (ULIRGs)** are the results of the work carried out by me at the Indian Institute of Astrophysics, Bengaluru and the Indian Institute of Science Education and Research, Pune, under the supervision of Prof Mousumi Das and the same has not been submitted elsewhere for any other degree.

_____
Prof Mousumi Das

_____
Sowkhya Shanbhog

ನನ್ನ ಕಣ್ಣುಗಳಲ್ಲಿ ತಮ್ಮ ಕನಸನ್ನು ತುಂಬಿಕೊಂಡು,
ನನ್ನ ಬದುಕಿನ ಕಾವ್ಯಕ್ಕೆ ಮುನ್ನುಡಿ ಬರೆದ ಸೋನಿಯ ಪ್ರೀತಿಯ ತಾತನಿಗೆ...

Acknowledgments

I'd like to express my heartfelt gratitude to the following individuals for their contributions to my master's journey and the successful completion of my thesis.

Thank you to my supervisor, Prof Mousumi Das, for providing me with guidance, encouragement, and support throughout the process. I am grateful to Prof Ramana Athreya for his expertise and insights as a member of my thesis committee, assisting me with project logistics, and being a source of inspiration throughout my journey.

I want to take this opportunity to express my sincere gratitude and appreciation to Dr Sumana Nandi for her invaluable support and guidance throughout my thesis. Thank you for allowing me to build on your work and providing the necessary resources and expertise to conduct my research effectively. I am grateful to my mentor, Dr Rubinur Khatun, for always being available to assist me when I was stuck and for your invaluable advice.

I want to express my gratitude to Prof Seema Sharma, Prof Ishwara Chandra, Prof Prasad Subramanian, Prof Sudipta Sarkar and Prof Ramon Brasser for their assistance in my early efforts.

Sudheera H V, Shalini Sudheer, and Surya Shanbhog, my Pappa, Amma and little brother, thank you for being so strong and supporting me during the most difficult times. I am blessed to have my best friends, Chahana Nagesh and Prajnadipt Ghosh, for being the most significant source of comfort and strength during the challenging times.

And a special thanks to the IISER family for their financial assistance during the unprecedented times. Finally, I want to express my gratitude to my friends and family for their unwavering support, love, and encouragement throughout this journey. This thesis would not have been possible without your presence, for which I am eternally grateful.

x

Contents

List of Figures

List of Tables

Abstract

ULIRGs, or Ultra-Luminous Infra Red Galaxies, are incredibly bright galaxies that emit intense Infra Red (IR) radiation due to the merger of two gas-rich galaxies. The intense star formation due to the merger generates a significant amount of ultraviolet radiation, absorbed by surrounding dust and re-emitted in the IR range, making galaxies look very bright at this wavelength. Observations of the galaxies show that they are evolving into elliptical galaxies.

While star formation is the primary source of energy for ULIRGs, it has been discovered that nearly half of all ULIRGs detected also contain active galactic nuclei (AGNs). Furthermore, ULIRGs are considered the low-redshift counterparts of distant radio-loud galaxies, making them a valuable research topic. Understanding the behaviour of AGN in these galaxies is critical for studying our nearby Universe and its cosmological consequences.

Despite extensive research on ULIRGs at optical and IR wavelengths, detailed radio maps of these galaxies have not been studied. In this study, we intend to make radio frequency maps of a sample of ULIRGs, enabling us to observe their radio morphologies and search for extended features like jets. We will also determine the emission's spectral index, turnover frequency and break frequency, which will provide vital information about the physical processes taking place within these galaxies. The break frequency will enable us to calculate the spectral age of the ULIRGs, helping us understand where it stands in the evolution of radio-loud galaxies.

We find that ULIRGs have a low-frequency turnover comparable to Compact Steep Spectrum (CSS) sources, which are thought to be young radio sources that evolve into large radio galaxies. The measured spectral ages have a median of around 3 million years. This age is younger than large radio relic galaxies that are $10^7 - 10^8$ million years old. This fits with the claim that ULIRGs are new radio sources. The radio powers at 1.4 GHz is very near to $\log P_{1.4\text{GHz}} = 25$, the radio power that separates Fanaroff–Riley I and Fanaroff–Riley II radio sources.

Chapter 1

Introduction

This chapter aims to contextualise the thesis's work. We'll talk about how galaxies were discovered, and galaxy evolves (section 1.1), introduce ULIRGs and their characteristics at different wavelengths (section 1.2), introduce radio astronomy (section 1.3), comprehend synchrotron emission and go over the concept behind calculating out the synchrotron age (section 1.4).

1.1 Island Universes

Harlow Shapley and Heber Curtis debated 'the Scale of the Universe' at the Smithsonian Museum of Natural History in 1920. Shapley considered the Milky Way to be the entire Universe, with nebulae, or faint, fuzzy, cloud-like patches of light in the sky, located on the outskirts of our galaxy. On the other hand, Curtis claimed that the nebulae were 'island universes' similar to our Milky Way and that the Universe was larger than Shapley claimed.

Edwin Hubble's studies of the Andromeda Nebula brought 'the Great Debate' to a close. Hubble used the 100-inch Hooker telescope to resolve individual stars in this nebula. Hubble discovered Cepheid variable stars in Andromeda, which vary in brightness and can be used to measure distance (as discovered by Henrietta Leavitt in 1912). Hubble calculated that Andromeda was approximately 860,000 light-years away using Leavitt's formula. That's more than eight times the distance between the Milky Way's most distant stars. This demonstrated that the Andromeda nebula was a distinct star system and that our galaxy is not the entire Universe.

After discovering galaxies, Hubble proposed a simple classification system (Figure 1.1) based on their morphology. He realised that galaxies generally fall into one of three categories: spiral galaxies, elliptical galaxies, and irregular galaxies. Hubble classified spiral galaxies, disk-like galaxies with spiral arms, into two types based on the presence (SB-type) or absence (S-type) of a central bar. He further classified them based on how tightly or loosely (type -a to -c) the arms were bound. Lenticular galaxies were disc galaxies that lacked spiral arms (S0-type). The galaxies without any internal structure were called elliptical galaxies (E-types) and were further classified based on their ellipticities.

The irregular galaxies did not fit into the previously described categories. They were usually caused by the collision of two galaxies. The tuning fork classification was confused to also be the evolutionary sequence of galaxies in which 'early type' elliptical galaxies evolve into 'late type' spiral galaxies [1]. Galaxies are now believed to evolve in the exact opposite direction.
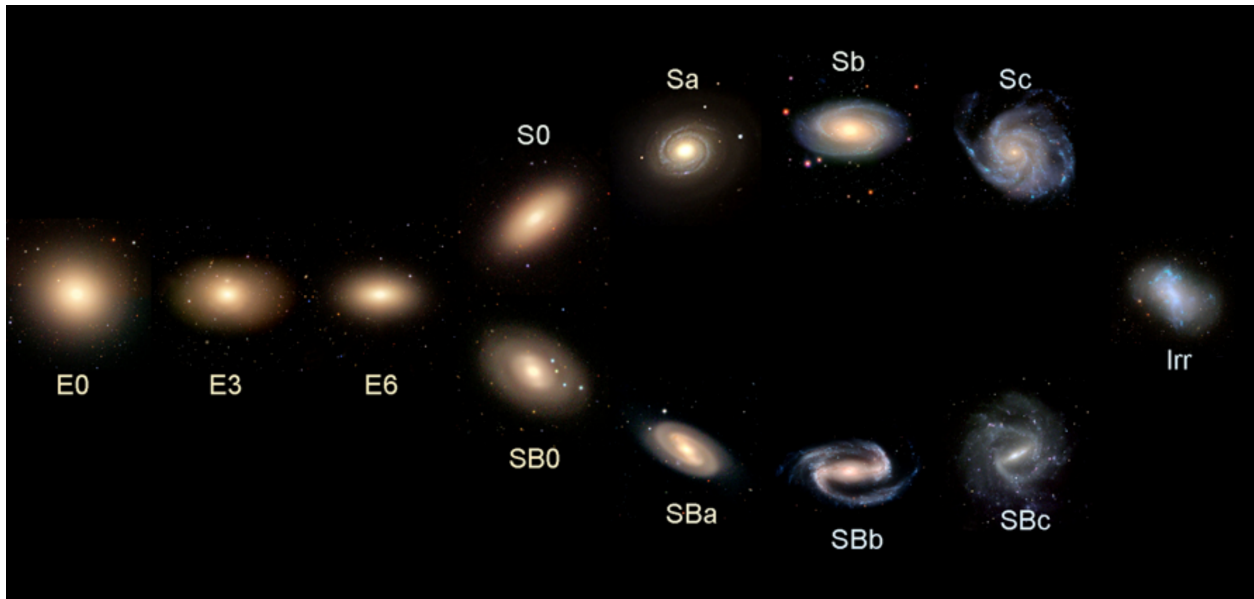
Figure 1.1: Hubble's Tuning Fork. *Image Credits: Department of Physics, University of Oregon*

1.1.1 Galaxy-Galaxy Interaction

Galaxies can exist in a variety of configurations. They can be solitary or part of a tiny group, like the Milky Way, Andromeda, and the dwarf galaxies that join them in our Local group. Alternatively,

---

[1]Hubble warned [1] that the nomenclature is just to distinguish the positions of the galaxies in the classification sequence and any implications of tuning fork on the evolution sequence must be done at one's peril

they can form larger clusters, such as the Virgo cluster, where more number of galaxies are grouped together.

Galaxies can be gravitationally bound to one other. The gravitational attraction can drive galaxies to drift closer together over time. When two galaxies approach each other, their gravitational pull strengthens, and the galaxies may merge. The merging event, in turn, modifies the gravitational potential between the galaxies, resulting in significant structural changes. Tidal tails, which are elongated streams of stars and gas stripped from galaxies during a collision, and virialisation, which is the process of establishing a stable equilibrium state by randomising the velocities of stars due to gravitational forces, are examples of these changes. Furthermore, such collisions can cause intense processes like starburst and Active Galactic Nuclei (AGN) activity.

The cloud-cloud collisions during the merger send shock waves through the clouds, causing them to collapse. The collapsed clouds form stars, triggering intense star formation or starburst. The starburst's luminosity primarily derives from the young massive stars generated in the burst. The gas can also be fueled into the central Super Massive Black Hole (SMBH), resulting in the formation of AGNs. The supermassive black holes of the interacting galaxies merge at the end stage, triggering radio jets. The AGN's luminosity is caused by the dissipation of gravitational energy released by gas falling upon the SMBH.

1.2   Ultra Luminous Infra Red Galaxies

The Infra Red All-Sky Survey (IRAS) found a new class of galaxies that contained more energy in the Infra Red (IR) part of their spectrum than at all other wavelengths. Called the Ultra Luminous Infra Red Galaxies (ULIRGs), they have IR brightness between $10^{12} L_\odot < L_{IR(8-1000\mu m)} < 10^{13} L_\odot$ [2], probably making them one of the brightest objects in the Universe. Even though they are sparsely present in the local Universe, they are a hundred times more numerous at $z > 1$ [3], making them an essential component in understanding galaxy formation and evolution.

Follow-up observations of almost all (95%) ULIRGs are interacting/merging gas-rich spiral galaxies with smaller separations between the merging galaxies than LIRGs[2] [2]. Near-IR spectroscopy

---

[2] The class Luminous Infra Red Galaxies (LIRGs) have luminosities $10^{11} L_\odot < L_{IR(8-1000\mu m)} < 10^{12} L_\odot$. There is also a class of galaxies with luminosities $L_{IR(8-1000\mu m)} > 10^{13} L_\odot$ called the Hyper Luminous Infra Red Galaxies (HyLIRGs)
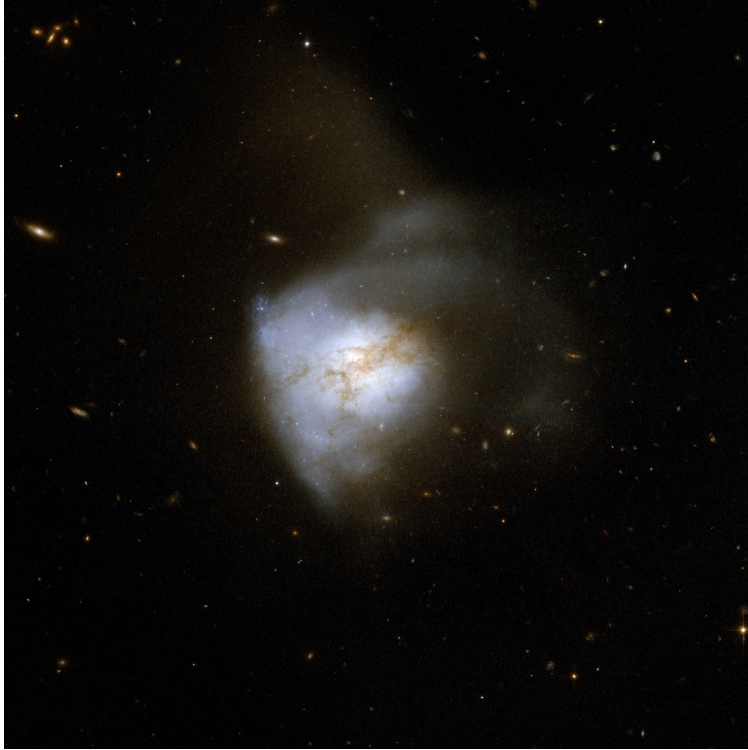
Figure 1.2: Arp 220 is one of the nearest ULIRG to Earth. It is formed by the merging of two galaxies. *Image Credits: NASA, ESA, the Hubble Heritage (STScI/AURA)-ESA/Hubble Collaboration, and A. Evans (University of Virginia, Charlottesville/NRAO/Stony Brook University)*

shows that ULIRG mergers are ellipticals in formation [4]. It also showed that around 25% of ULIRGs show evidence for an AGN, and the fraction increases with increasing IR luminosity (reaching $\sim 50\%$ at $L_{IR} > 10^{12.3} L_{\odot}$) [3]. The energy source for ULIRGs is intense star formation associated with the merger process and active galactic nuclei (AGNs). The dust absorbs the emission from the starburst (and AGN if present) and re-emits in IR, making them extremely bright in IR.

Hence, observations and simulations suggest that ULIRGs may represent a phase of the evolution of the galaxies (Figure 1.4). The dust and gas-rich mergers trigger starburst and AGN activity. The feedback from these energetic events blows away the dust to reveal a quasar. Once the quasar fades, the system virialises into an elliptical galaxy. Studying AGNs in ULIRGs helps us learn the formation of quasars from gas-rich galaxies.

Figure 1.3: A selection of Luminous Infra Red galaxies (LIRGs) from the Great Observatories All-sky LIRG Survey(GOALS). Most of the LIRGs are merging 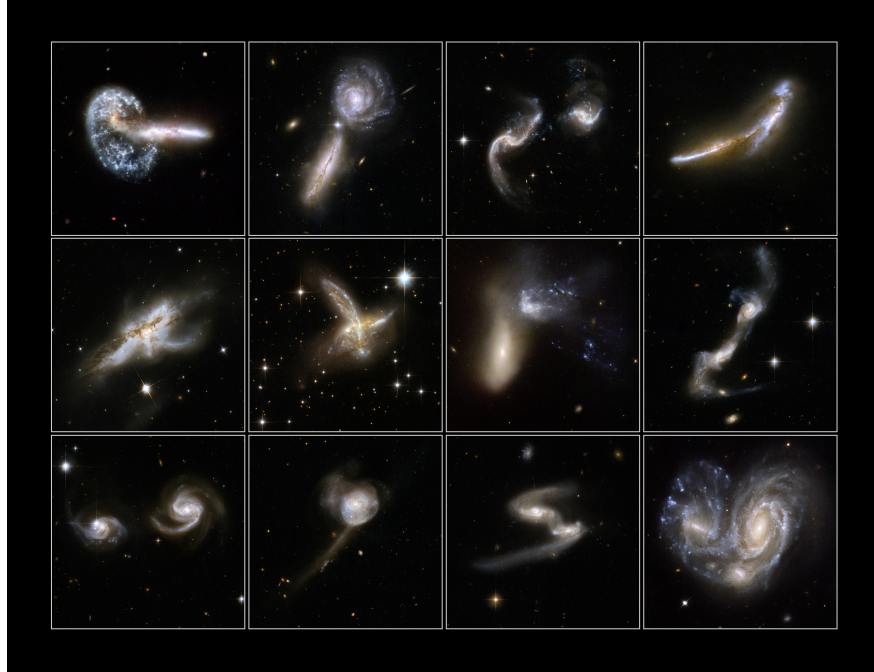galaxies. *Image Credits: NASA/ ESA/ STScI/AURA (The Hubble Heritage Team) - ESA/Hubble Collaboration/ University of Virginia, Charlottesville, NRAO, Stony Brook University (A. Evans)/ STScI (K. Noll)/ Caltech (J. Westphal)*

1.2.1   Multi-wavelength Observations of ULIRGs

Multiwavelength observations of ULIRGs are necessary to understand the different complexities it hosts. The colour composite in Figure 1.5's centre is composed of wavelengths of IRAS 08572+3915 ranging from the far-UV to the near-IR as blue-to-red and reveals diverse aspects of the system.

One of the two merger nuclei and young super-star clusters along the leading edge of one of the tidal tails dominate the ultraviolet (UV) emission. Massive young stars radiate strongly in the UV region. This is because a star's temperature is inversely proportionate to its mass. And because of their higher energy production and quicker depletion of their fuel reserves, massive stars also have shorter lives than smaller ones, making far-UV light an ideal tool for detecting new star formation[3].

However, most of the radiation that smaller stars release is in the optical and IR ranges, so when observing at these wavelengths, we have a greater chance of finding older stars that have been

---

[3]For main sequence stars of mass M and luminosity L, $L \propto M^{3.5}$. The lifetime t of main sequences stars $t \propto M^{-2.5}$

The Evolutionary Merger Scenario

Spiral Galaxies → Interaction / Early Stage Merger LIRG → Late Stage Merger ULIRG → Quasar → Elliptical Galaxy
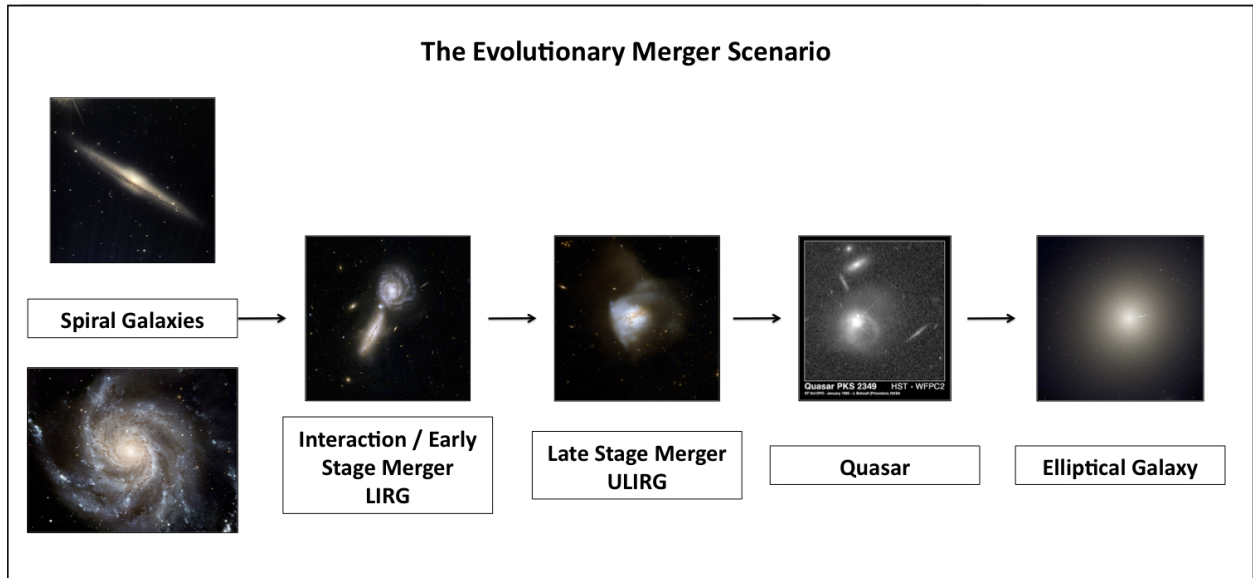
Figure 1.4: Diagram depicting the merger scenario, in which two gas-rich spirals merge to form a LIRG, which evolves into a ULIRG, then a Quasar, and finally an elliptical galaxy. *Image Credits: CANDELS collaboration blog*

around for a longer time. We can see the merger galaxy body, which appears to be two spirals with tidal tails at optical wavelengths, which are dominated by old stars.

At mid-IR, we trace line emission from warm dust heated by young stars. All emission sources other than an emission source in the North-West nucleus fade away as we move into the thermal IR. At thermal IR, we detect black body continuum emission from dust heated by young stars (or AGN if present).

Dust grains scatter and absorb photons at optical and UV wavelengths but are too small to affect radio waves. As a result, astronomers can use radio wavelengths to look deeper into dust-covered objects to see what is hidden.

1.3 Jansky's Merry-Go-Round

At Bell Laboratories, Karl Jansky discovered the first radio signal from space while investigating various sources of static noise on his antenna. The extraterrestrial radio 'hiss' was later linked to a
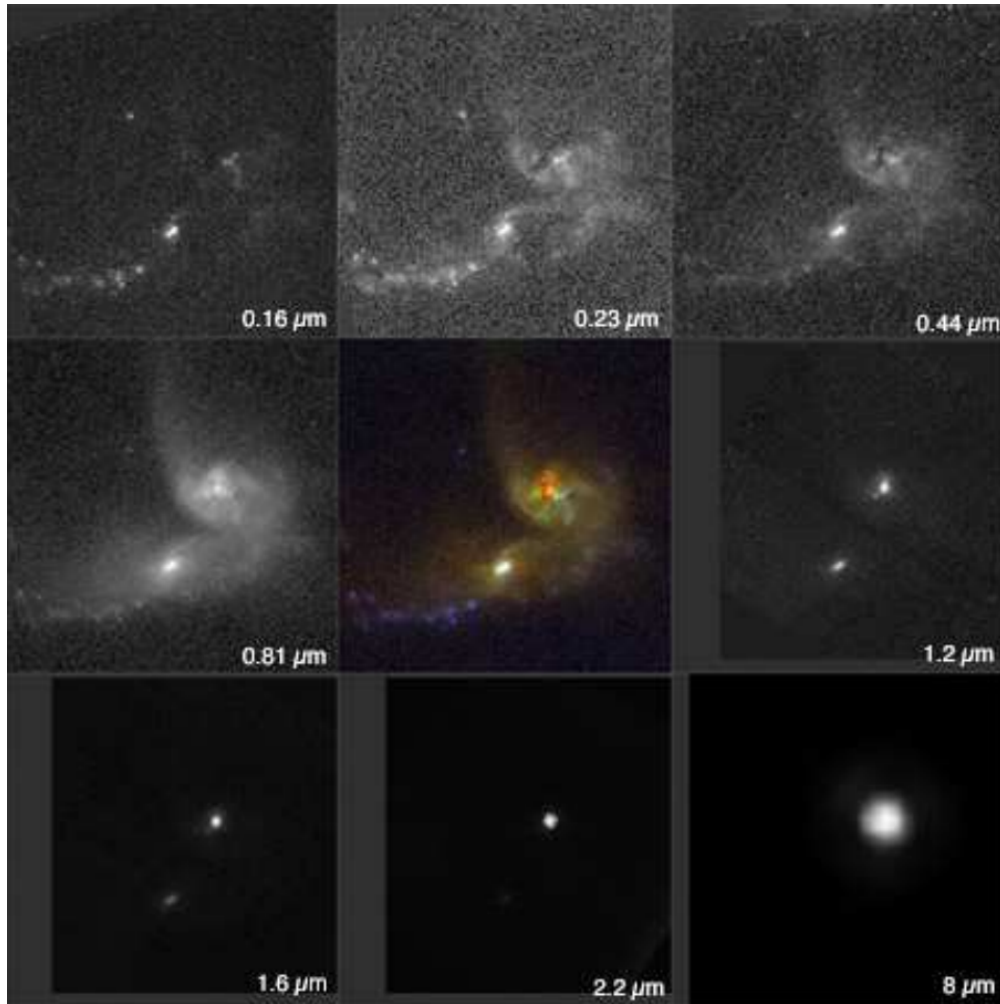
Figure 1.5: IRAS 08572+3915 at various wavelengths from far UV on the top left to far IR on the bottom right. The images from 0.16 - 2.2μm are from various instruments on Hubble Space Telescope. The 8μm image is from Spitzer Space Telescope. *Image Credit: From [3] in which the author compiled images from various sources cited within*

source near the centre of our Milky Way galaxy.[4] To honour his contribution, the unit of radio flux density is named after him.

$$1\,\text{jansky} = 10^{-26}\,\text{W}\,\text{m}^{-2}\,\text{Hz}^{-1}$$

This gives us the impression that the flux density we measure in radio astronomy has a tiny order

---

[4]Did you know that, since Karl Jansky first began studying the radio sky, the combined power of all radio telescopes is insufficient to light a light bulb for even a single second?

7

of magnitude.

There are two basic mechanisms for radio emission: thermal and non-thermal radiation. Thermal radiation occurs in all bodies whose temperature is above Absolute Zero. When electrons in the medium are in thermal equilibrium, the thermal motion emits black body radiation at the temperature T_b, the same temperature as that of the electrons. For thermal sources peaking in radio emission, the flux density can be given by the Rayleigh-Jeans (RJ) law.

$$S = \frac{2kT_b}{\lambda^2} d\Omega \tag{1.1}$$

Here,

- $k = 1.380649 \times 10^{-23}\,\mathrm{m^2\,kg\,s^{-2}\,K^{-1}}$ is the Boltzmann constant

- T_b is the black body temperature or the brightness temperature

- λ is the wavelength of light

- $d\Omega$ is the infinitesimal solid angle

The equation predicts that the thermal emission flux densities at radio wavelengths are minimal, and the radio sky is dark and empty. But observations have revealed that radio sources emitting flux densities are much higher than predicted by the RJ Law through non-thermal processes like the synchrotron mechanism (See Section 1.4).

1.3.1   Aperture synthesis and Radio Interferometer

The Rayleigh criterion states that the angular resolution of a telescope is diffraction limited and is given by λ/D, where D is the aperture size, and λ is the wavelength. We can achieve higher resolution by building larger telescopes (an engineering challenge) and operating at shorter wavelengths. The radio wavelengths are so long that even though the radio telescopes are large, the resolution is very poor. For comparison, the resolution of a ground-based optical telescope is limited to 1" due to atmospheric effects. To achieve a resolution of 1" by observing the 21 cm (HI) line, one would need a telescope that is 43 km in diameter.

Consider a massive parabolic dish (Figure 1.6). A parabolic dish coherently adds parallel light rays. When some segments of the parabola are deleted, this remains. Place the remaining segments on the ground. We can coherently combine the signals with proper delays as long as we know exactly where the segments are. This technique of aperture synthesis is used by radio astronomers to achieve high resolution.
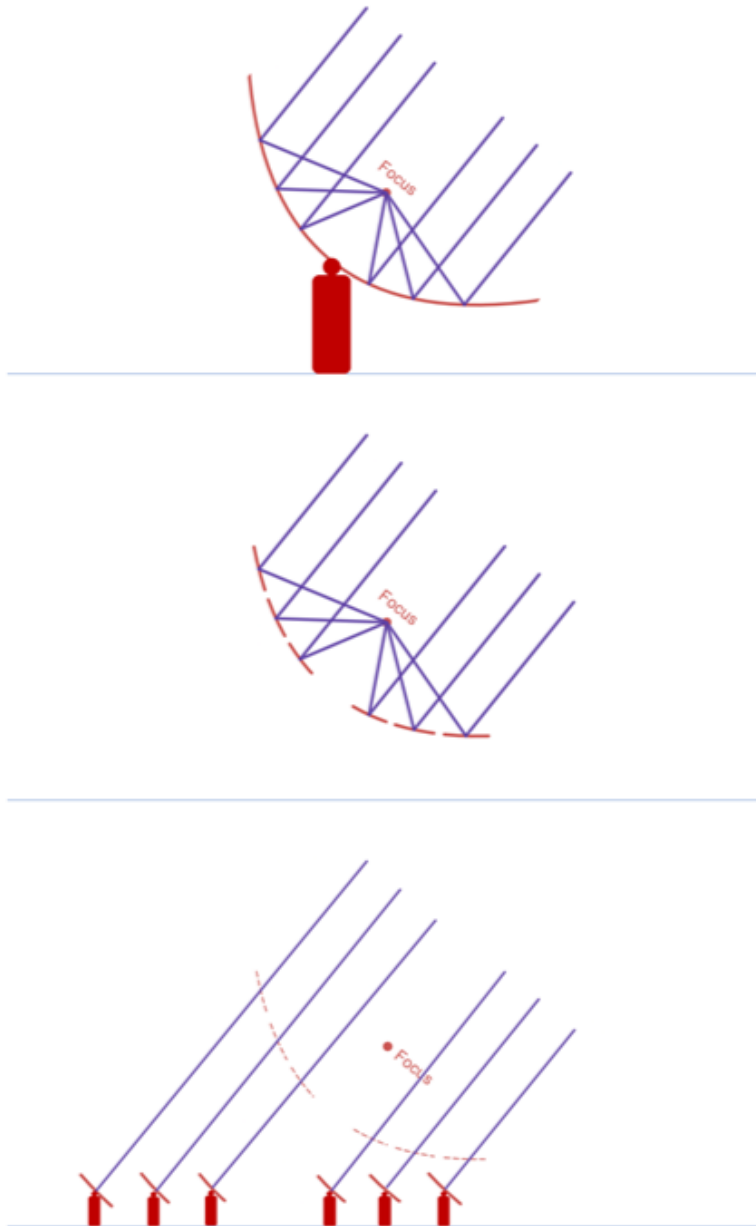
Figure 1.6: Aperture Synthesis imagined in a simple diagram

The method of aperture synthesis resembles the double-slit experiment with quasi-monochromatic light and a radio two-element interferometer. The output voltages are correlated to obtain 'visibility'.

The Van Cittert Zernike (VCZ) Theorem relates the visibilities $V(u,v)$, where (u,v) are baseline coordinates, to the distribution of intensity on the sky $I(l,m)$, where l,m are the direction cosines on the sky, via a Fourier transform.

$$V(u,v) = \mathscr{F}\{I(l,m)\} \tag{1.2}$$

Figure 1.7: The 'Wye' of the Very Large Array(VLA) at New Mexico with 27 dishes making an effective dish of 4 km in diameter at its widest configuration *Image Credit: NRAO/AUI/NSF*

Correlation of the voltages from any two radio antennas then allows the measurement of a single Fourier component of the source brightness distribution. Given a sufficient number of measurements, the source brightness distribution can be obtained by Fourier inversion (See Section 3.1).

1.4   Synchrotron Radiation

Accelerating charged particles emit radiation. Acceleration by a magnetic field produces 'magneto bremsstrahlung', the German word for magnetic braking radiation. The particle will radiate

according to the Larmor formula, which for relativistic particles is,

$$P = \frac{dW}{dt} = \frac{2q^2}{3m^2c^3}\gamma^2 \left(\frac{d^2\mathbf{p}}{dt^2}\right) \tag{1.3}$$

where $\gamma = \frac{1}{\sqrt{1-v^2/c^2}}$ is the Lorentz factor, c is the speed of light, q is the charge of particle, m is the mass of the particle, $\mathbf{p}$ is the momentum of the particle. From Equation 1.3 ($P \propto m^{-2}$). Lightest charged particles (electrons and positrons, if any are present) are hence accelerated more than relatively massive protons and heavier ions, so electrons (and possibly positrons) account for virtually all of the radiation observed.

Ultrarelativistic electrons (kinetic energies $\gg m_e c^2$) produce synchrotron radiation when they gyrate in the presence of a magnetic field due to Lorentz's force. The observed spectrum is the convolution of the electron energy distribution with the spectrum of an individual electron. We get a power law energy distribution $S_\nu \propto \nu^{-\alpha}$ when the energy distribution of electrons is a power law, $N(E) \propto E^{-\gamma}$.
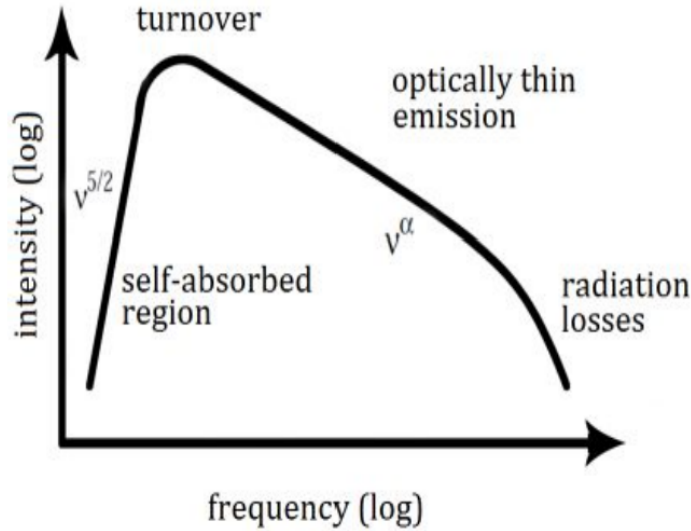
Figure 1.8: A generic synchrotron spectrum *Image Credits: Multifrequency study of GHz-peaked spectrum sources and candidates with RATAN-600 radio telescope, Group IAG*

The synchrotron spectrum deviates from the power law under different circumstances, as seen in Figure 1.8. Thermodynamically, no region can emit incoherent radiation with intensity greater than that of a black body at its thermodynamic temperature given by the RJ Law given by Equation

1.1 [5]. The synchrotron radiation's brightness temperature at lower frequencies may approach the electrons' kinetic temperature. When this occurs, synchrotron self-absorption becomes important. The calculation gives a steep spectrum $S_\nu \propto \nu^{5/2}$ at low-frequencies.

The synchrotron spectrum evolves with time as the electrons radiate away their energy. The electron with higher energies (higher frequencies) loose energy faster. This results in a break in the power law spectrum at break frequency ν_{br}, which shifts to lower frequencies with time. The position of the ν_{br} will help us interpret the age of electrons and estimate the source's lifetime.

Chapter 2

Radio Continuum studies of ULIRGs

2.1 Why Radio Astronomy?
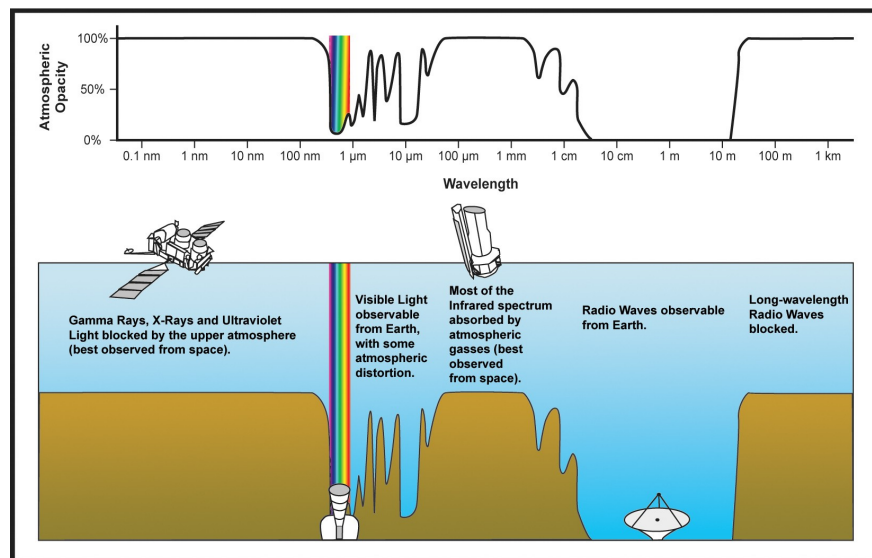
Figure 2.1: Atmospheric Electromagnetic Transmittance shows that the optical wavelengths are affected by the atmosphere, and IR wavelengths have no transmittance. The radio wavelengths are not obstructed by the atmosphere. *Image credits: NASA*

The Earth's atmosphere has different transmittance rates to different wavelengths (See Figure 2.1). The atmosphere is opaque to IR radiation, compelling us to use space-based observatories to study the universe in IR. The IR space-based telescopes, until recently with the launch of JWST, have

13

very low resolution. We can see this in Figure 2.2, which displays the observations made at multiple wavelengths of ULIRG ARP 220. The optical wavelengths are also affected by the atmosphere and the dust present in the ULIRGs. These reasons make it difficult to probe the small-scale nuclei of ULIRGs using these wavelengths. Whereas radio wavelengths are unaffected by the presence of dust, and with the help of aperture synthesis and interferometric techniques, the small-scale nuclei can be probed at high resolutions. The nuclei of ARP 220 have been observed with the highest resolution in the radio wavelengths.
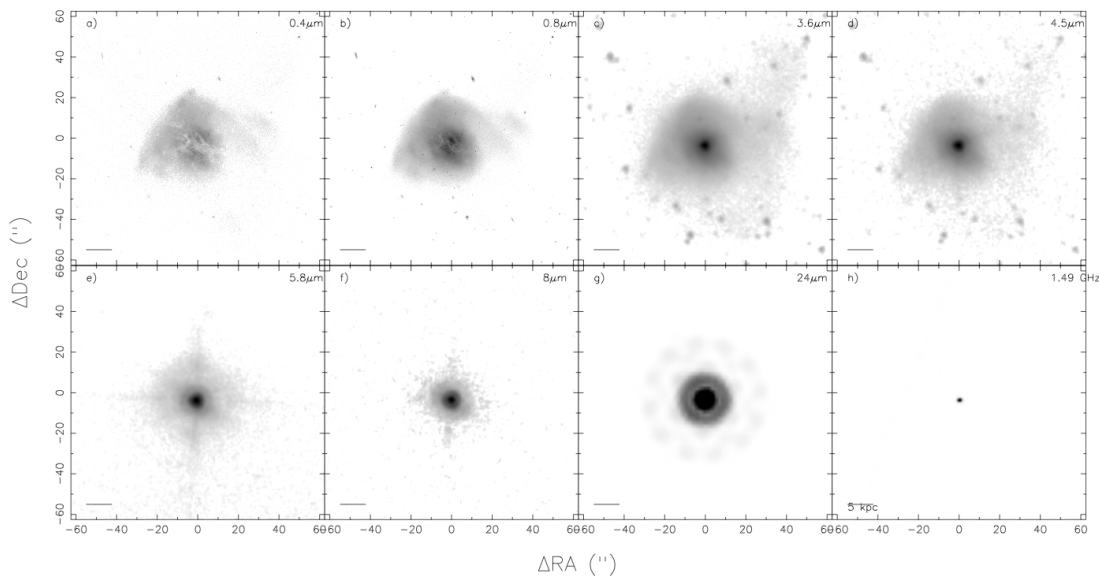
Figure 2.2: ARP 220 observed in optical($0.4 - 0.8\mu m$), IR ($3.6 - 24\mu m$) and radio ($1.4 GHz$). Radio interferometers like VLA are capable of probing into the dusty nucleus of the ULIRG at higher resolution(*Image Credits: Great Observatories All-sky LIRGs Survey (GOALS)*)

The radio continuum emission from galaxies is linked to the massive stars. As discussed before in Section 1.2.1, massive stars emit strongly in UV wavelengths, and probing massive stars help us understand star formation. These high-energy photons ionise the gas surrounding the massive
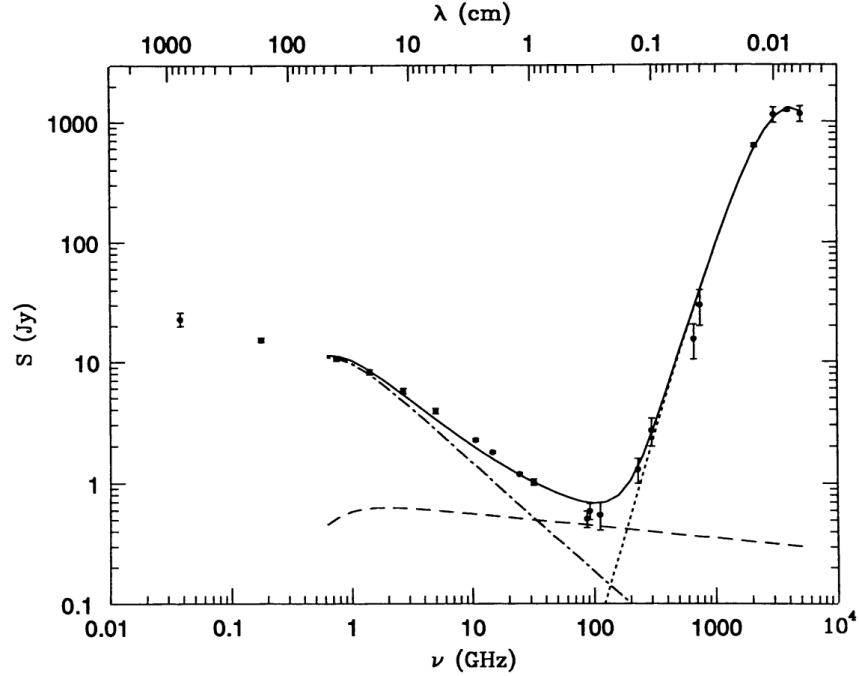
14

Figure 2.3: The spectrum of the starburst galaxy M82. It is the sum (solid line) of three emission components: synchrotron (dot dash line), thermal free-free (dashed line), cold dust (dotted line)

stars. The electrons in the plasma might scatter off ions, resulting in an acceleration, to emit 'free-free radiation' (the electrons are 'free' both before and after scattering). Massive stars also undergo supernovas, emitting synchrotron radiation. Figure 2.3 shows the combined spectrum of a star-burst galaxy [6] with synchrotron radiation, free-free radiation and cold dust emission. As the free-free emission and synchrotron emission occur in radio wavelengths, radio continuum emission helps us probe star formation too.

If AGNs are present, the strong magnetic fields also accelerate the electrons to emit synchrotron emission. These emissions are confined very close to the supermassive black holes of the galaxies, and hence the emission is very compact. When the emission region is optically thick (like the region below 1 GHz in Figure 2.3, causing a 'turnover' in the emission), the emission can be approximated to a black-body emission to calculate the brightness temperature T_b given by the RJ law (Equation 1.1). If this temperature is greater than the temperature of HII regions (clouds of hydrogen gas ionised by young massive stars) of $\sim 10^4$ K [7], the emission can be confirmed to be coming from a non-thermal source. AGNs can be hence identified by compact emission with high brightness temperature T_b.

2.2 AGNs in ULIRGs

The optical spectral studies show that the energy sources in ULIRGs are a mix of starburst and active galactic nuclei (AGN). It is hypothesised that these ULIRGs are the dust-enshrouded phases of quasars. These nuclei become 'optically chosen' quasars once they shed the dust. [8]

Radio continuum studies of AGNs mainly addressed the question if AGNs or supernovae were the dominant power sources in ULIRGs. It is shown that around 25% of ULIRGs show evidence for an AGN, and the fraction increases with increasing IR luminosity (reaching $\sim 50\%$ at $L_{IR} > 10^{12.3} L_{\odot}$) [3]. ULIRGs are observed to show similar relation between radio core power and bolometric luminosity as radio-quiet quasi-stellar objects (QSOs)[9]. Radio-quiet AGNs are $\sim 10^3$ times less powerful and do not have visible jets or lobes like their radio-loud counterparts [10].

The contribution of buried AGN to the radio emission of ULIRGs in a study showed that ULIRGs have a common radiative process regardless of the presence or absence of an optical AGN, suggesting AGNs might be equally contributing to the emission in all ULIRGs [11]. Although most of the emission was explained by star formation, some ULIRGs showed high non-thermal emission and high spectral break frequency, suggesting the presence of AGNs.

A survey of ULIRGs showed they had a flat spectral index from 1.49 to 8.49 GHz [12]. The flat spectrum was suggested to be due to high electron density. A follow-up survey from 1.4 to 22.5 GHz showed that there was steeping on the high-frequency end of the spectrum, and was attributed to electrons loosing energy through synchrotron emission [13].

2.2.1 Gigahertz Peaked Sources and Compact Steep Spectrum sources

The radio sources are categorised based on the turnover frequency in their radio spectrum [14]. Sources with $\log P_{1.4\text{GHz}} \geq 25$, compact ($\leq 1\text{kpc}$) and radio spectrum peaking around 500 MHz - 10 GHz is called Gigahertz Peaked-Spectrum (GPS) radio sources. Sources with similar power, larger in size (1 - 20 kpc) and peaking $< 500\,\text{MHz}$ are called Compact Steep-Spectrum (CSS) radio sources.

The morphology of GPS and CSS sources is observed to be similar to large radio galaxies [15]. GPS and CSS sources could be early phases of powerful large-scale radio sources. Various evo-

lutionary models [16, 17, 18] also supported the argument that GPS, CSS and large radio galaxies are an evolutionary sequence.

We can compare the radio properties of GPS/CSS sources with that of ULIRGs to understand if ULIRGs are similar to GPS/CSS sources and hence part of the evolutionary sequence of radio galaxies.

2.2.2   Fanaroff-Riley (FR) classification

Based on the relative locations of the high and low brightness in the lobes of the radio sources, B.L. Fanaroff and J.M. Riley developed the Fanaroff-Riley (FR) classification.

As one approaches the lobe's outer extremities, the FRI sources grow fainter, and the spectra become steeper, indicating that the high-energy radiating particles have lost most of their energy. These sources are hence 'aged'. They are generally seen in rich clusters of galaxies. The jets are two-sided, subsonic, with a distorted plume-like structure.

The FRII sources have their lobes' hotspots further away from the centre. They are not usually found in clusters. The jets are supersonic, one-sided due to relativistic beaming and smooth with hotspots at the end of the well-defined lobes.
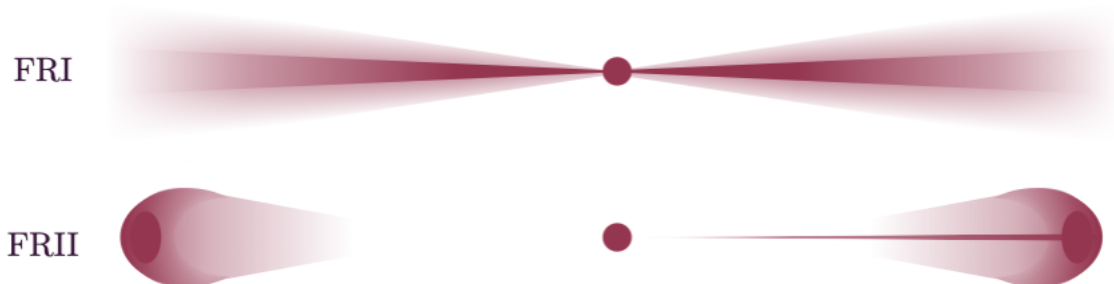

Figure 2.4: The traditional Fanaroff Riley classification of radio galaxies. FRI galaxies are "centre-bright", and FRII galaxies are "edge-brightened" (often with "hotspots" towards the edge). *Image Credits: Emma L. Alexander*

The differences in the classification might suggest that they are intrinsically different from each

other, but it can also be possible that the FRII sources loose energy over time to evolve into FRI sources [19]. The host galaxies look like ellipticals, but observations show that their morphologies are rather complicated, with the presence of dust and disk-like structures interacting with each other.

One of the dichotomies is related to radio power at 1.4 GHz. The FRI sources have $\log P_{1.4\text{GHz}} \leq 25$ and FRII sources have $\log P_{1.4\text{GHz}} \geq 25$. This division occurs near the break in the radio luminosity function of radio galaxies when it is modelled as a broken power-law function, leading to the theory that these two populations of radio galaxies correspond to different populations of cosmologically evolving sources. [20].

This dichotomy can be used on ULIRGs to understand their relationship with the FR classification and, in turn, understand where ULIRGs lie in the sequence of evolution of radio galaxies.

Chapter 3

Methods

3.1 Radio Data Analysis

From the VCZ-theorem, we know that if the image $I(l,m)$ is represented as a discrete 2D function, it can be represented as the Fourier transform of the visibilities $V(u,v)$.

$$I(l,m) = \sum_{u,v=-\infty}^{\infty} V(u,v)[\cos(2\pi(ul+vm)) - i\sin(2\pi(ul+vm))]\delta u \delta v \qquad (3.1)$$

$$V(u,v) = \sum_{l,m=-\infty}^{\infty} I(l,m)[\cos(2\pi(ul+vm)) - i\sin(2\pi(ul+vm))]\delta l \delta m \qquad (3.2)$$

The complex sinusoidal function's amplitude indicates the intensity of a specific frequency component, whereas the phase information describes where the power must be put. The image is rebuilt due to the waves' constructive and destructive interference.

The telescope arrays sample different points in the UV plane according to the (u,v) coordinates. The (u,v) coordinates depend on the baseline, i.e., the distance between the arrays and the hour angle of the phase centre. Hence, as the Earth rotates, the $(u.v)$ points trace out tracks, sampling more of the UV plane.

The Fourier transform of the UV plane is called the PSF or the Dirty beam, or the diffraction

pattern of the aperture (See Figure 3.1).
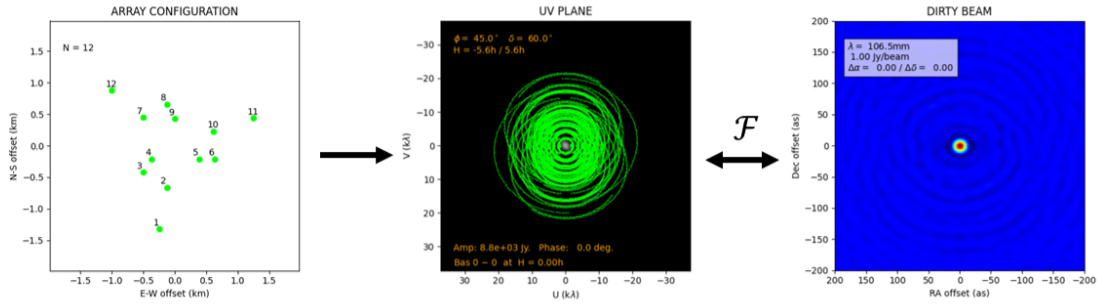
Figure 3.1: Each antenna pair measures visibility in the UV plane. The Fourier transform of the measured visibilities is the Point Spread Function (PSF) or the Dirty Beam of the antennas. *Image Credits:* `APSYNSIM`[21]

The PSF convolved with the true sky image (I^{true}) produces the image of the sky. This image is called the Dirty Image (I^D) (See Figure 3.2).

$$I^D = PSF * I^{true}$$
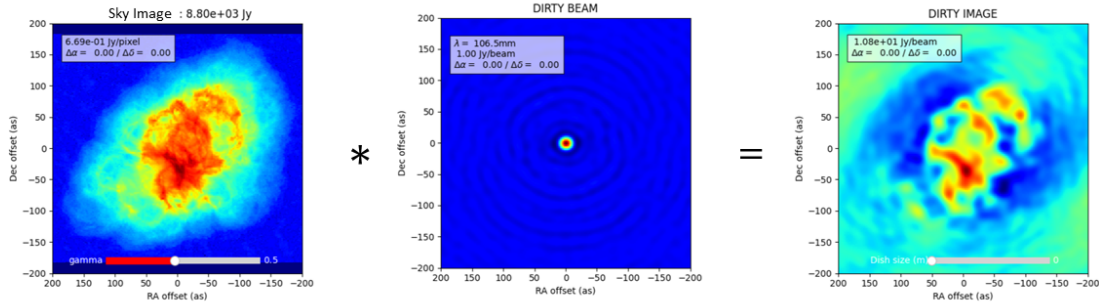
Figure 3.2: The Dirty Beam convolved with the True sky gives the Dirty Image. This is what we observe with the telescope. *Image Credits:* `APSYNSIM`[21]

The above equation is true only for an ideal noise-less system. The true sky image could have been easily obtained with the help of properties of Fourier transform and Convolution theorem properties.

$$I^{true} = \mathscr{F}^{-1}\left\{ \frac{\mathscr{F}\{I^D\}}{\mathscr{F}\{PSF\}} \right\}$$

20

But in reality,

$$I^D = PSF * I^{true} + \varepsilon$$

where ε is the noise. Hence, to deconvolve the image, various algorithms are used. One of them is called Högbom `CLEAN`. The algorithm has the following assumptions:

- Most of the sources in the radio sky are point-like and can be modelled as delta functions

- The sky is sparsely filled with such sources
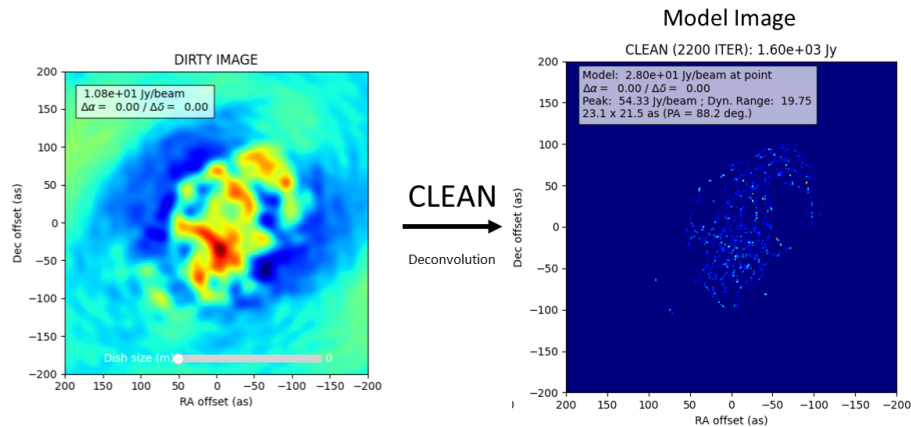
Figure 3.3: The Dirty Image is deconvolved or `CLEAN`-ed to get a Model Sky Image, a collection of delta functions of the brightest pixels in the Dirty Image. *Image Credits: `APSYNSIM`[21]*

The algorithm follows these steps:

1. Find the brightest pixel in the dirty image.

2. 'Transfer' the peak flux multiplied by the gain factor to a Model Image. Subtract the peak flux by the dirty beam and a gain factor < 1 from the dirty image. (See Figure 3.3)

3. Repeat steps 1 and 2 until a residual flux threshold or a number of iterations is reached. What is left of the dirty image is called Residual Image.

21

4. Convolve the Model Image with an Ideal `CLEAN` beam. We obtain the Restored image (See Figure 3.4). The idealised beam is usually an elliptical Gaussian with the same shape and size as the inner part of the array dirty beam.

5. Add the residual image from step 3 to the restored image to get the final image. (See Figure 3.5)

Figure 3.4: The model sky image is convolved with an Ideal PSF or the `CLEAN` Beam to get a `CLEAN` Restored Image. *Image Credits: APSYNSIM [21]*

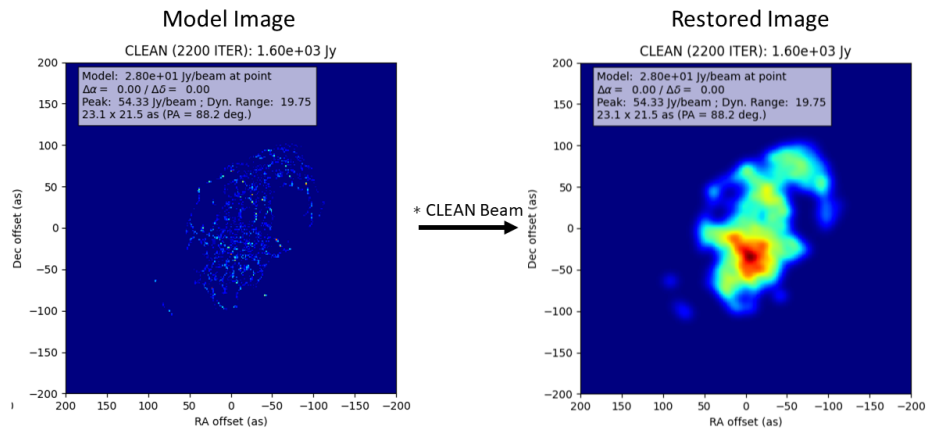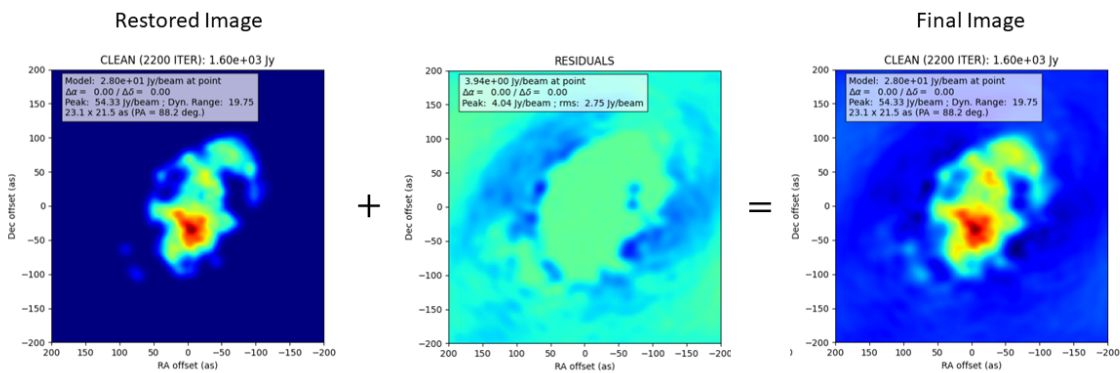Figure 3.5: The residuals from the `CLEAN` can be added to the restored image so that no emission is missed. *Image Credits: APSYNSIM [21]*

3.1.1 Calibration

Radio waves can be considered plane waves, described as a vector of complex numbers, as the cosmic sources are very far from us. The transverse plane wave propagating in the z-direction does not have a z-component, and the x and y-components are the same across the wavefront.

$$\vec{e} = \begin{bmatrix} e_x \\ e_y \end{bmatrix}$$

The amplitudes of the components of the signal are given by the Stokes Parameters.

$$I = \langle e_x e_x^* \rangle + \langle e_y e_y^* \rangle$$

$$Q = \langle e_x e_x^* \rangle - \langle e_y e_y^* \rangle$$

$$U = \langle e_x e_y^* \rangle + \langle e_y e_x^* \rangle = 2Re(\langle e_x e_y^* \rangle)$$

$$V = -i(\langle e_x e_y^* \rangle - \langle e_y e_x^* \rangle) = 2Im(\langle e_x e_y^* \rangle)$$

The I component is the total intensity. The Q and U components represent the linear polarisation component, and V represents the circular polarisation component.

The wave $\vec{e}$ travels from its source to our telescopes, passing through mediums like the interstellar medium, the Earth's atmosphere, and so on. The signal changes as it travels through a medium. We assume that these propagation's effects are linear. Thus, we can represent the propagation effect of each medium as a matrix causing linear transformation of the signal.

$$\vec{e}' = \begin{bmatrix} j_{11} & j_{12} \\ j_{21} & j_{22} \end{bmatrix} \vec{e} = J\vec{e}$$

The matrix J is called the Jones matrix. When there are multiple propagation effects, the total effect is just the matrix multiplication of all the Jones matrices multiplied in the order of propagation[1]. When it enters the antenna, it is recorded as two complex voltages.

---

[1]The order of the matrices can be changed in special cases. For example, Jones matrices that are scalar commute with all other matrices and hence can be multiplied to the signal at any stage.
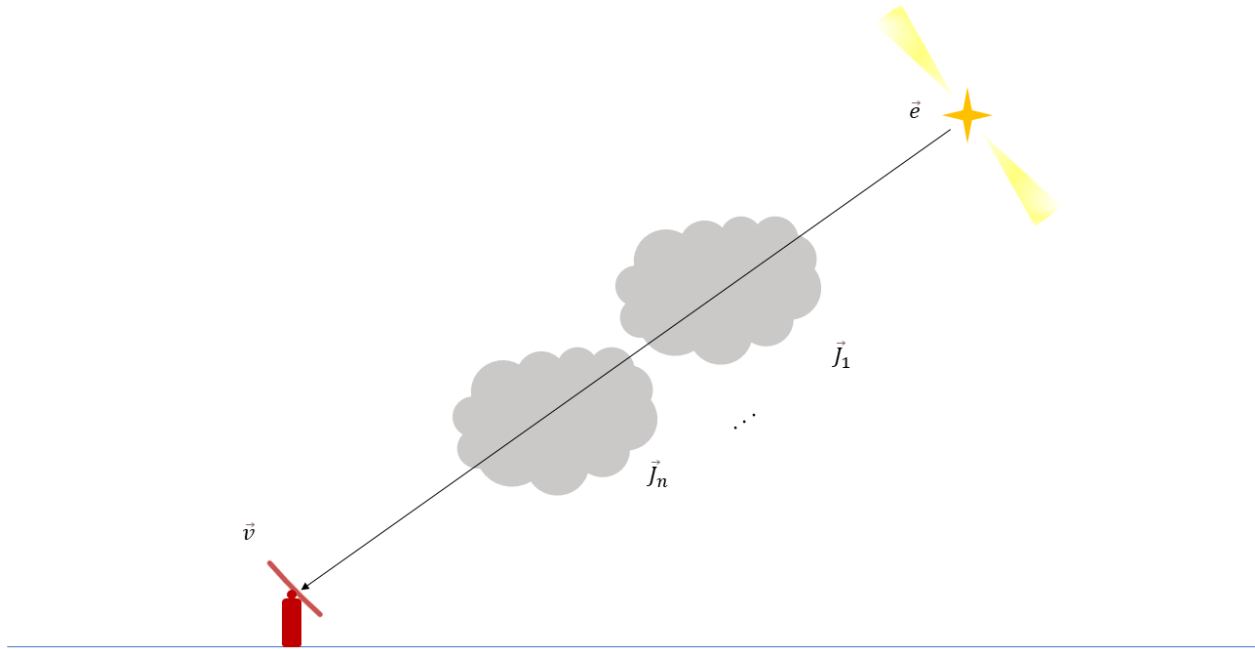
Figure 3.6: Propagation of Radio Wave

$$\vec{v} = \begin{bmatrix} v_1 \\ v_2 \end{bmatrix} = J_n J_{n-1} ... J_1 \vec{e}$$

For two antennas p and q,

$$\vec{v_p} = J_p \vec{e}$$

$$\vec{v_q} = J_q \vec{e}$$

The correlators in the telescope compute the complex products of the signals called correlations. The angular brackets represent averaging over time and frequency.

$$v_{11} = \langle v_{p1} v_{q1}^* \rangle$$

$$v_{12} = \langle v_{p1} v_{q2}^* \rangle$$

$$v_{21} = \langle v_{p2} v_{q1}^* \rangle$$

$$v_{22} = \langle v_{p2} v_{q2}^* \rangle$$

It is convenient to represent the correlations as a matrix.

$$V_{pq} = 2 \begin{bmatrix} v_{11} & v_{12} \\ v_{21} & v_{22} \end{bmatrix} = 2 \langle \vec{v_p} \vec{v_q}^H \rangle$$

Where H is the hermitian of the vector. We will assume that the Jones matrices are constant over the averaging interval.

$$\begin{aligned} V_{pq} &= 2 \langle \vec{v_p} \vec{v_q}^H \rangle \\ &= \langle J_p (2 \vec{e} \vec{e}^H) J_q^H \rangle \\ &= J_p \langle 2 \vec{e} \vec{e}^H \rangle J_q^H \\ V_{pq} &= J_p B J_q^H \end{aligned}$$

The above equation is called the Radio Interferometer Measurement Equation (RIME), where B is called the Brightness matrix. All the science is contained in this matrix.

$$B = \begin{bmatrix} I+Q & U+iV \\ U-iV & I-Q \end{bmatrix}$$

In the real world, there is an additional noise term to the RIME,

$$V_{pq} = J_p B_{pq} J_q^H + N_{pq}$$

We have to now estimate the J's so that we can get the B's. We will look at sources whose properties we already know from past observations for this. These sources are known as calibrators, and their RIME is as follows:

$$V_{pq}^{cal} = J_p B_{pq}^{cal} J_q^H + N_{pq}$$

Knowing V_{pq}^{cal} and B_{pq}^{cal}, we can calculate the Jones matrices, which can then be used in the RIME of

our source to obtain the true signal of our source. The Jones matrices cover a large array of effects from atmospheric effects, parallactic angle effect of motion of the sky, etc. But the electronics effects, bandpass response and geometric effects are the most important calibrations to be done. The types of calibrators used to calculate these effects are:

- Flux Calibrator

  - Flux calibrator is used to set the flux scale of the observations as it is a source of well-known flux density, as the interferometer cannot measure the absolute flux.
  - It is preferred to be a point source but can be extended.

- Bandpass Calibrator

  - Bandpass Calibrator is used to calibrate the frequency response of the system as the telescope is not uniformly sensitive to all frequencies.
  - Bandpass is engineered to be constant over time and hence can be solved over large time intervals.
  - As bandpass has a complicated frequency structure, it is solved over small frequency intervals. Hence, the calibrator needs to be bright, with a well-known spectrum, to keep the calibration errors down.
  - Often the same as the flux calibrator

- Gain Calibrator

  - Gain Calibrator is used to derive complex gains to correct the relative temporal variation of the phase of the associated signal on the antennas.
  - It varies over time and is hence observed more frequently over the observing run. The solution interval is over the whole frequency band at short intervals of time.
  - The calibrator needs to be close to the source of interest and is highly preferred to be a point source.

3.2   Calculating Synchrotron Age

We (S Nandi et al. in prep) choose 8 ULIRGs from IRAS 1 Jy Survey [22]. It contains ULIRGs whose $60\mu m$ flux density is greater than 1 Jy from the IRAS Faint Source Catalog. We compiled

the flux densities of these sources from the works of literature and surveys. `SYNAGE` software [23] was used to fit the radio spectrum through these flux densities to obtain the turnover frequencies, break frequencies and spectral indices to calculate the spectral ages of the ULIRGs. All ULIRGs emit compact radio emissions and have a constant influx of new relativistic particles [24]. As a result, we used the continuous injection (CI) approach for spectral fitting. We use α as a free parameter for fitting. (Refer to Appendix A for the derivation of the equations below.)

We will calculate the spectral ages and turnover frequencies to understand if there is any evolutionary connection between ULIRGs, GPSs and CSSs.

We will also calculate the radio power at 1.4 GHz for all these ULIRGs to understand their relation to Fanaroff–Riley I and Fanaroff–Riley II classified radio sources [25].

Source	z	D_L (Mpc)	S_0 (Jy)	v_0 (MHz)	$S_{1.4\text{GHz}}$ (Jy)
IRAS 01569-2939	0.1397	652.6	0.490	200	0.124
IRAS 05156-3024	0.1718	819.3	0.062	200	0.019
IRAS 05189-2524	0.0428	186.8	0.002	1510	0.029
IRASF 07599+6508	0.1480	695.2	0.100	408	0.042
IRAS 10494+4424	0.0921	416.6	0.022	1400	0.022
IRAS 11119+3257	0.1876	903.5	0.540	408	0.110
IRAS 12127-1412	0.1330	618.6	0.081	1400	0.081
IRAS 13428+5608	0.0373	162.1	0.145	1400	0.145

Table 3.1: Data of ULIRGs gathered from literature and archives

3.2.1 Calculations

The minimum magnetic field is hence given by Equation A.26 in convenient units [26],

$$B_{min}(\mu G) = 10^6(1+z)\left(\frac{4.67 \times 10^{-20}(1+k)}{f_s \phi \theta_x"\theta_y"s}\int_{v_l}^{v_u}\frac{S_v}{v^{1/2}}dv\right)^{2/7} \tag{3.3}$$

- z is the redshift

  – z is obtained for all galaxies from NASA/IPAC Extragalactic Database (NED)

27

- k is the ratio of the relativistic proton to relativistic electron energy

    - We will assume the relativistic electron and proton have similar energy $k = 1$

- f_s is the shape factor for the volume emission region. For a cylinder, it has the value $\pi/4$

- ϕ is the volume filling factor

    - We will assume the source is uniformly filled with relativistic particles and magnetic field $\phi = 1$

- θ_x", θ_y" the dimensions of the source were measured either using `SAOImageDS9` [27] or `CASA imview` [28] (see Figure 3.7)

- s is the depth of source inputted in kpc.

- ν_l is the lower cutoff frequency in MHz

- ν_u is the upper cutoff frequency in MHz

- S_ν is flux density inputted in mJy

- Frequency ν is substituted in MHz

The lifetime of electrons in the radio component undergoing both synchrotron radiative and inverse Compton losses due to cosmic microwave background (CMB) photons is given by [29],

$$\tau_{syn}(\text{Myr}) \approx 50.3 \frac{B_{min}^{1/2}}{(B_{min}^2 + B_R^2)[(1+z)\nu_{br}]^{1/2}} \tag{3.4}$$

- $B_R \simeq 0.318(1+z)^2$ in nT is magnetic field equivalent to the radiation, which was assumed to be predominantly Cosmic Microwave Background photons

- ν_{br} is the break frequency in GHz

    - Four ULIRGs in our sample, IRAS 05156-3024, IRAS 05189-2524, IRAS 10494+4424, and IRAS 12127-1412, have a very large break frequency from the spectral fitting. Hence, for the spectral age calculations, we e using the highest frequency we have flux for the spectral age calculations.
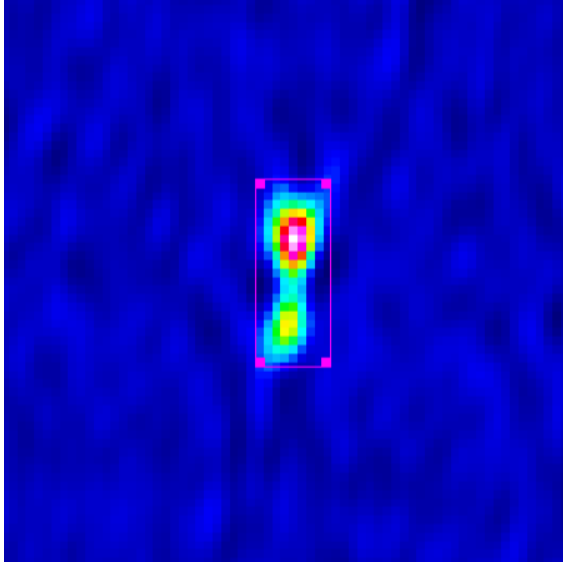
(a) Radio image of IRAS 05189-2524 at 8.49 MHz is an extended source. We recorded w and l for this source
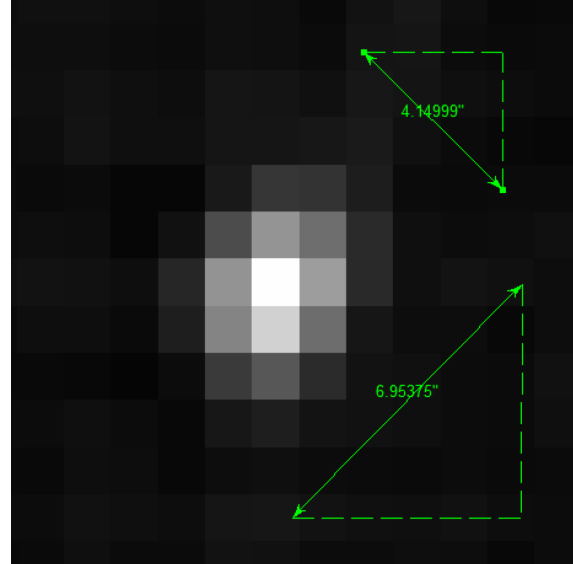
(b) Radio image of IRAS 05156-3024 is a point source at 3 GHz. The measured w and l was averaged for this source

Figure 3.7: Measuring the dimensions of the Radio Sources

- B_{min} is the minimum magnetic energy from Equation 3.3 inputted in nT

The radio contours of the 8 ULIRGs sample were overplotted on Pan-STARRS r-band optical image to correlate the radio and optical image. The radio contours are plotted according to the RMS noise level in the image 3.2. The contours range in multiples of 3σ (Refer Figure 4.3 to Figure 4.8)

Source	ν (MHz)	RMS Noise μJ/beam
IRAS 01569-2939	8460	96.2
IRAS 05156-3024	3000	157.1
IRAS 05189-2524	8490	73.7
IRASF 07599+6508	8460	88.3
IRAS 10494+4424	1440	135.1
IRAS 11119+3257	8460	55.8
IRAS 12127-1412*	1400	
IRAS 13428+5608	14900	160.5
	8460	61.7

Table 3.2: The frequency at which the sources were observed for the overlay images below, along with the RMS noise for contours.*The radio contours for this source are not overlain because the resolution is very low.*

Chapter 4

Results

4.1 Spectral Fitting, Age Calculations and discussion of individual sources

The calculations of the spectral ages are summarised in the table below. The spectra of the ULIRGs, along with the optical-radio overlay, follow.

Source	ν_{max} (MHz)	α_{inj}	ν_{br} (MHz)	B_{min} (μG)	τ_{syn} (Myr)	$P_{1.4\text{GHz}}$ (W Hz^{-1})
IRAS 01569-2939	85.17	0.643	1510	22.9	10	24.7802
IRAS 05156-3024	-	0.722	>3000	17.4	<10.9	24.1576
IRAS 05189-2524	282.2	0.625	>8490	160	<0.27	23.0778
IRASF 07599+6508	118.3	0.549	1021	114.8	1.192	24.3559
IRAS 10494+4424	189.1	0.416	>1490	9.86	<35	23.6454
IRAS 11119+3257	356.4	1.000	639.3	278	0.39	25.0329
IRAS 12127-1412	166.2	0.375	>1400	3.3	<83	24.5343
IRAS 13428+5608	113.7	0.453	4822	27	4.7	23.6516

Table 4.1: Estimates of break frequency, spectral age turnover frequency, and radio power

IRAS 01569-2939

The source displays a highly distorted structure, which can be observed in the R and K' bands. A narrow tidal tail can be seen extending over 55 kiloparsecs, and a shorter counter-tail is likely

to be present on the west side of the object [30]. Only a single nucleus is identified in the object [31], which is classified as a Seyfert 1 [32]. The spectral characteristics of the object were obtained through the fitting, including an 85.17 MHz low-frequency turnover, a 1510 MHz break frequency, and a spectral age of 10 million years, as illustrated in Figure 4.1.
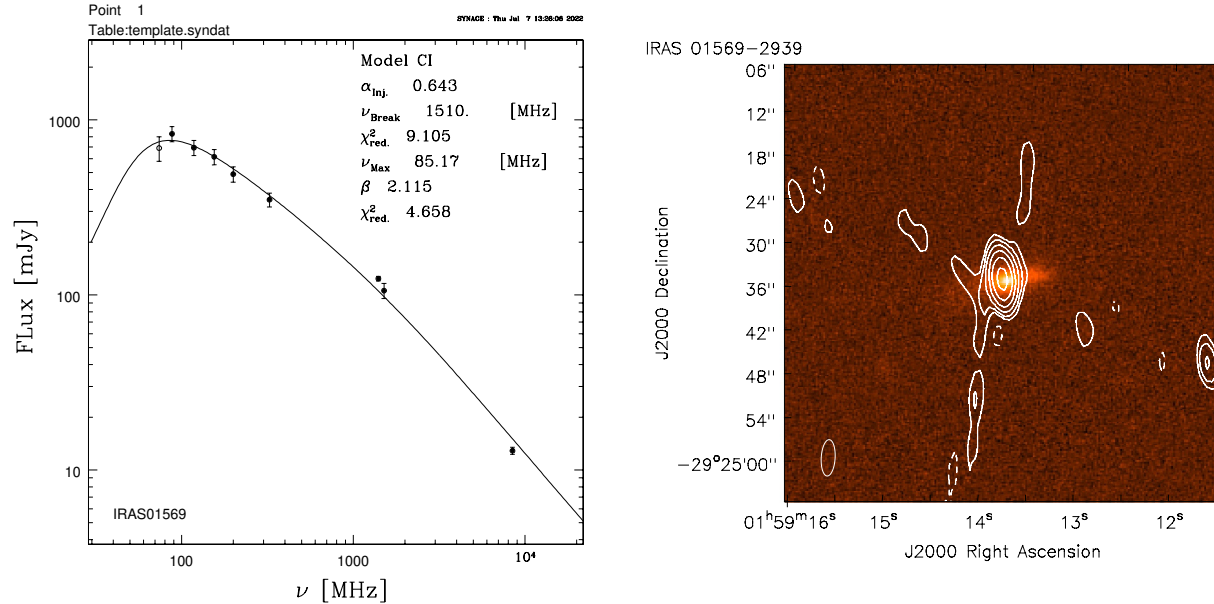

Figure 4.1: Radio Spectrum of IRAS 01569-2939 with their best fitting model is on the left panel. The vertical axis is the flux density in mJy, and the horizontal axis is the frequency in MHz in the log scale. 8.46 GHz VLA radio contours are plotted at $3\sigma[1, 1, 2, 4, 8, 16, 32, 64, 128]$ and overlaid on Pan-STARRS r-band optical image in the right panel

IRAS 05156-3024

The single-nucleus object under examination displays a brief tidal feature towards the southern region in both R and K' bands [30]. The optical spectrum of the object corresponds to that of a Seyfert 2 galaxy[33]. In the radio spectrum, no turnover frequency is observed, and the break frequency is extremely high, measuring 8.9×10^7 MHz, as depicted in Figure 4.2. The spectral age of the source has been calculated by considering the highest frequency available for flux measurement as the break frequency (refer to Table 4.1 for the selected ν_{br} for calculations). The resulting spectral age of the source is less than 10.9 million years.

IRAS 05189-2524

The Palomar Telescope optical images of the system exhibit two intersecting tails, indicating that
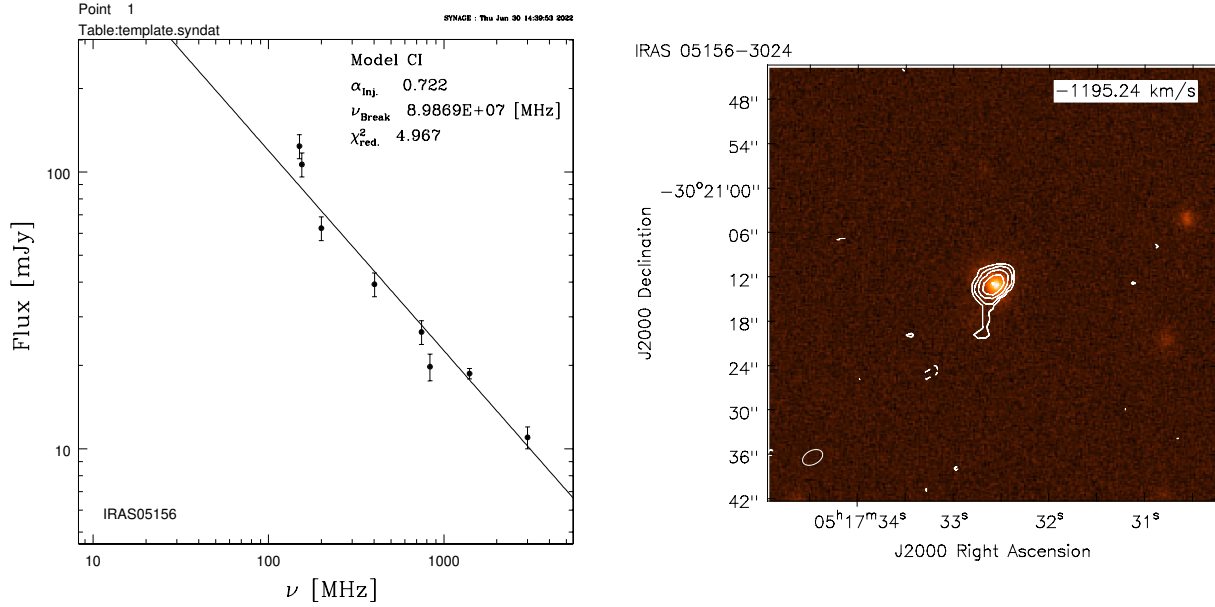
Figure 4.2: Radio Spectrum of IRAS 05156-3024 with their best fitting model is on the left panel. The vertical axis is the flux density in mJy, and the horizontal axis is the frequency in MHz in the log scale. 3 GHz VLASS radio contours are plotted at $3\sigma[1,1,2,4,8,16,32,64,128]$ and overlaid on Pan-STARRS r-band optical image in the right panel.

it is an evolved merger of two spiral galaxies [8]. In contrast, Hubble images of the system reveal off-centre nuclei, distorted outer sections, and a dim, arcing tail around the galaxies [34]. The system is classified as a Seyfert 2 galaxy [35]. It exhibits a low turnover frequency of 282.7 MHz and an extremely high break frequency, as determined through spectral fitting. Similar to the previous galaxy, we have considered the highest frequency available for flux measurement as the break frequency (refer to Table 4.1). The system is resolvable at a radio frequency of 8.49 GHz, as seen in Figure 4.3. The spectral age of the source is less than 0.27 million years, indicating that IRAS 05189-2524 is a relatively new source.

IRASF 07599+6508

The galaxy has broad line absorption lines and is categorised as a radio-quiet quasi-stellar object (QSO). Hubble images reveal clumps of emissions surrounding the QSO, which could be associated with emissions from massive stars and a recent star-forming event [36]. R and K' bands show the presence of tidal tails [30]. The system has a low-frequency turnover at 118.3 MHz and a break frequency of 1021 MHz. The spectral age of the ULIRG is 1.192 Myr. The 8.46 GHz VLA contours show extended radio emission from the source (See Figure 4.4).
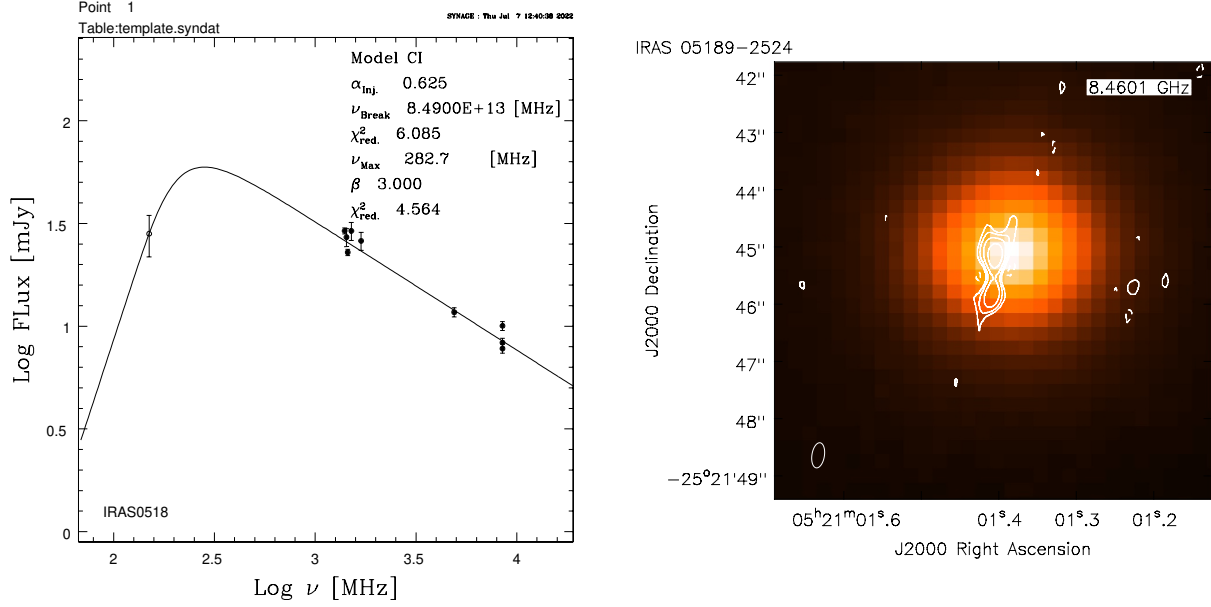
Figure 4.3: Radio Spectrum of IRAS 05189-2524 with their best fitting model is on the left panel. The vertical axis is the flux density in mJy, and the horizontal axis is the frequency in MHz. 8.49 GHz VLA radio contours are plotted at $3\sigma\,[1,1,2,4,8,16,32,64,128]$ and overlaid on Pan-STARRS r-band optical image in the right panel.

IRAS 10494+4424

IRAS 10494+4424 is a single-nucleus system. In optical, it is categorised as a LINER galaxy. According to optical and infrared photometric modelling, the system's ionising source is a starburst [37]. There are two 'spikes' evident in the R and K' bands. The spikes could be the source of the system's tidal tails [30]. The spectral fitting gives a low-frequency turnover at 189.1 MHz and a high break frequency of 1.4×10^7 MHz. We took the highest frequency we have flux for as the break frequency (See Table 4.1) to get the maximum spectral age. The maximum spectral age is 35 Myrs. The highest available frequency for the galaxy is 1.44 GHz FIRST image. Because high-resolution data for this source are not available, the volume may be overestimated in this instance, resulting in high spectral age.

IRAS 10494+4424 is a system with a single nucleus, and it is classified as a LINER galaxy in the optical spectrum. Based on optical and infrared photometric modelling, the system's ionizing source is a starburst [37]. The R and K' bands show two spikes, which could be the cause of the system's tidal tails [30]. The spectral analysis shows a low-frequency turnover at 189.1 MHz and a high break frequency of 1.4×10^7 MHz. To obtain the maximum spectral age, the highest
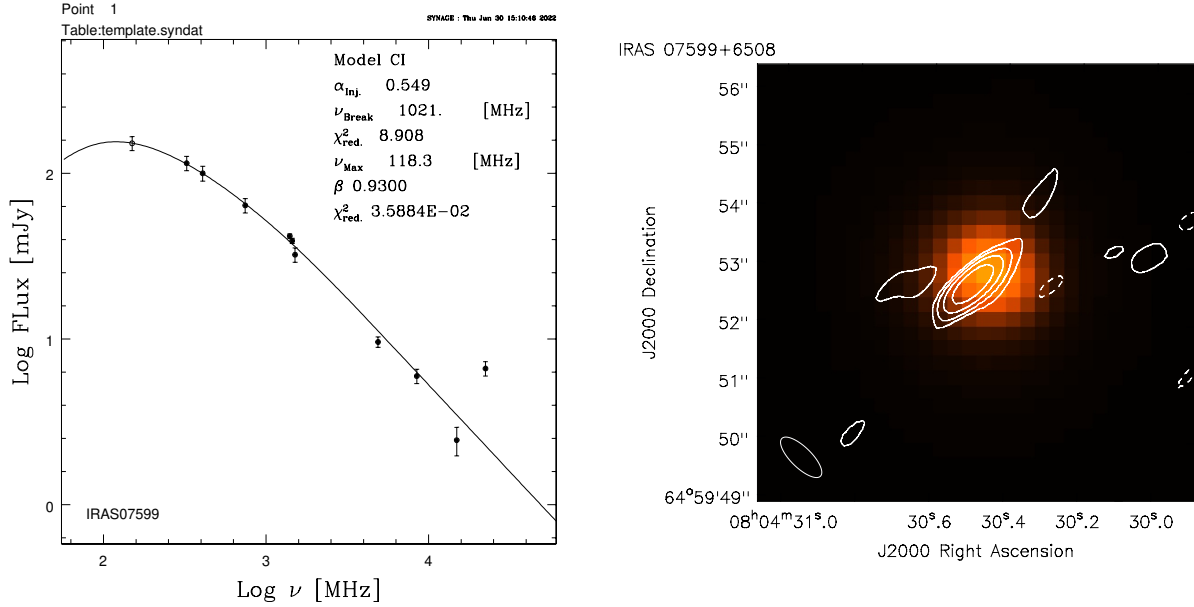
Figure 4.4: Radio Spectrum of IRASF 07599+6508 with their best fitting model is on the left panel. The vertical axis is the flux density in mJy, and the horizontal axis is the frequency in MHz. 8.46 GHz VLA radio contours are plotted at $3\sigma[1, 1, 2, 4, 8, 16, 32, 64, 128]$ and overlaid on Pan-STARRS r-band optical image in the right panel.

frequency available for flux measurements is taken as the break frequency, as per Table 4.1. The maximum spectral age of this system is 35 Myrs. The highest frequency data available for this galaxy is the 1.44 GHz FIRST image. The unavailability of high-resolution data for this source may lead to an overestimation of the volume, resulting in high spectral age.

IRAS 11119+3257

The R and K' band observations of the source reveal the presence of tidal tails [30]. It is categorized as a Seyfert 1 source [38]. The turnover frequency of the source is 356.4 MHz, and the break frequency is 639.3 MHz. The spectral age of the source is estimated to be 0.39 Myrs, indicating that it is a relatively young radio source. At a frequency of 8.46 GHz, the source exhibits extended emission (See Figure 4.6).

IRAS 12127-1412

The source is two merging galaxies where the members are widely separated [30]. It has a low-frequency turnover at 113.7 MHz and a break frequency at 4822 MHz. As the break frequency is high, to obtain the maximal spectral age, we used the highest frequency for which we have flux
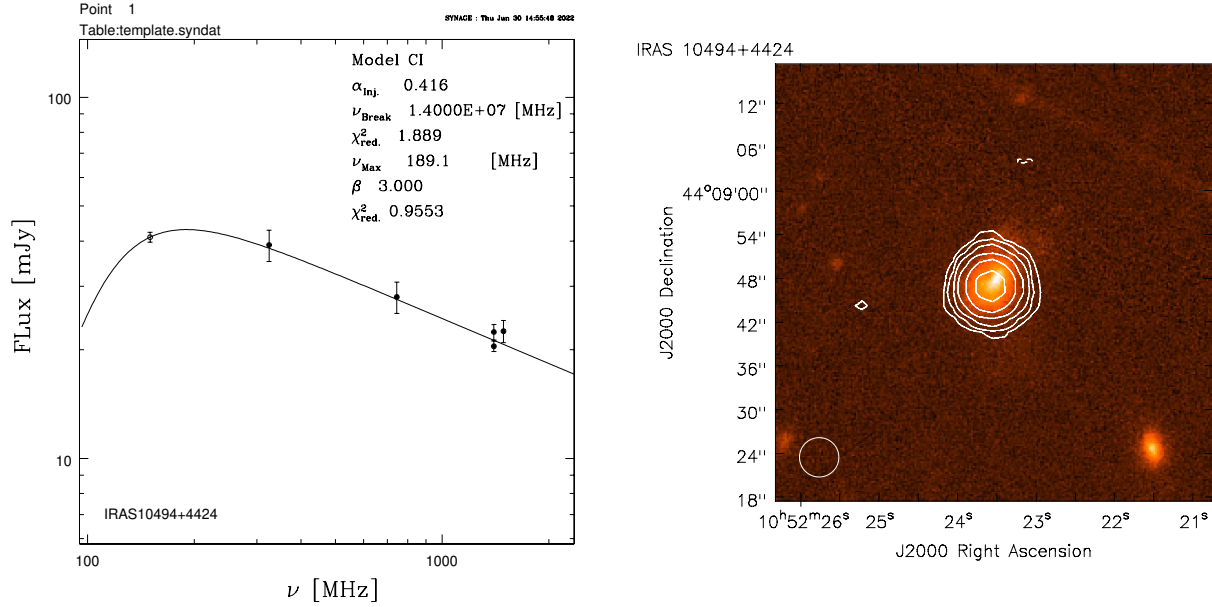
Figure 4.5: Radio Spectrum of IRAS 10494+4424 with their best fitting model is on the left panel. The vertical axis is the flux density in mJy, and the horizontal axis is the frequency in MHz in the log scale. 1.44 GHz FIRST radio contours are plotted at $3\sigma[1, 1, 2, 4, 8, 16, 32, 64, 128]$ and overlaid on Pan-STARRS r-band optical image in the right panel.

as the break frequency (See Table 4.1). The maximum spectral age is 83 Myrs. The galaxy's highest frequency image obtained is a 1.4 GHz NVSS image. Due to the lack of high-resolution measurements for this source, the volume may be overestimated, resulting in high spectral age.

IRAS 13428+5608

Also known as Mrk 273, this galaxy exhibits a striking tidal tail towards the south of the galaxy. At near-IR and radio wavelengths, what appears to be a single-nucleus object in UV/optical pictures resolves into a double-nucleus structure. It is categorised as a Seyfert 2 at optical frequencies and is a composite object powered by starburst and AGN activity [37]. Recent studies using LOFAR have newly detected arcs on the north with three resolved components in the nuclei [39]. The spectral fitting gives a low-frequency turnover at 113.7 MHz and a break frequency at 4822 MHz. The spectral age is 4.7 Myrs. In Figure 4.8, we can see that the source is resolved into two components at 8.46 GHz.
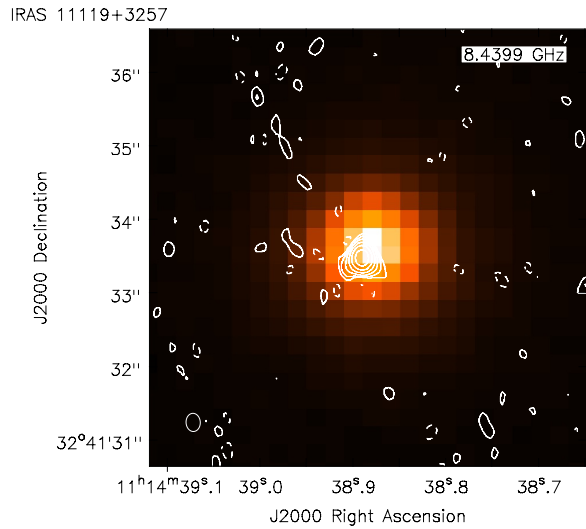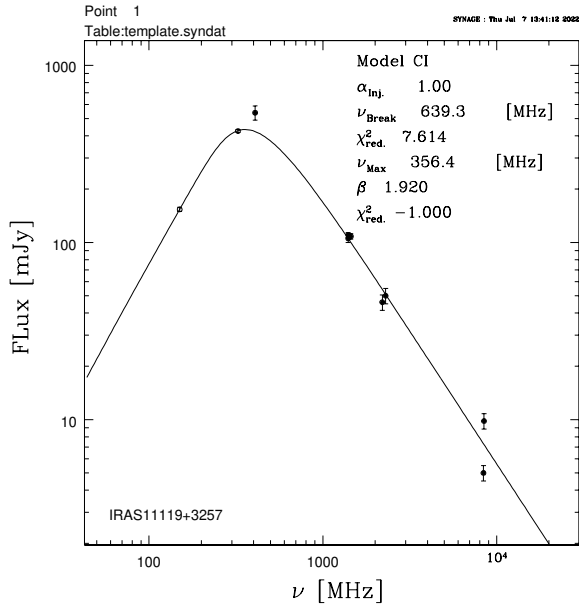
Figure 4.6: Radio Spectrum of IRAS 11119+3257 with their best fitting model is on the left panel. The vertical axis is the flux density in mJy, and the horizontal axis is the frequency in MHz in the log scale. 8.46 GHz VLA radio contours are plotted at $3\sigma[1,1,2,4,8,16,32,64,128]$ and overlaid on Pan-STARRS r-band optical image in the right panel
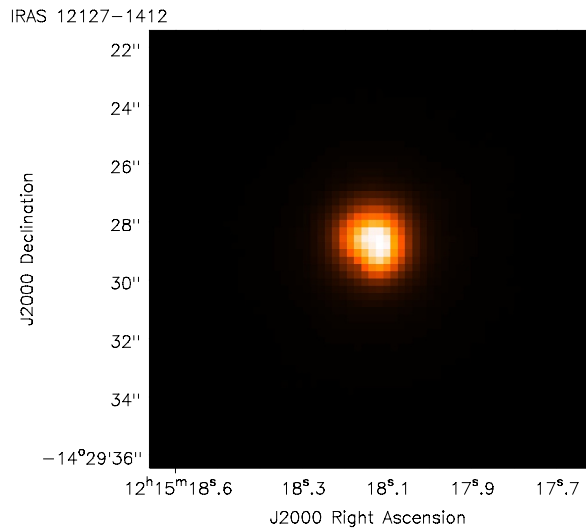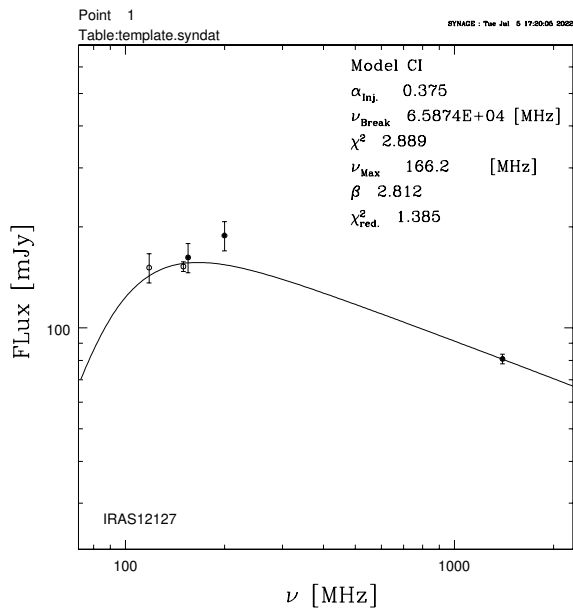

Figure 4.7: Radio Spectrum of IRAS 12127-1412 with their best fitting model is on the left panel. The vertical axis is the flux density in mJy, and the horizontal axis is the frequency in MHz in the log scale. Pan-STARRS r-band optical image in the right panel. The radio contours couldn't be plotted due to their low resolution.
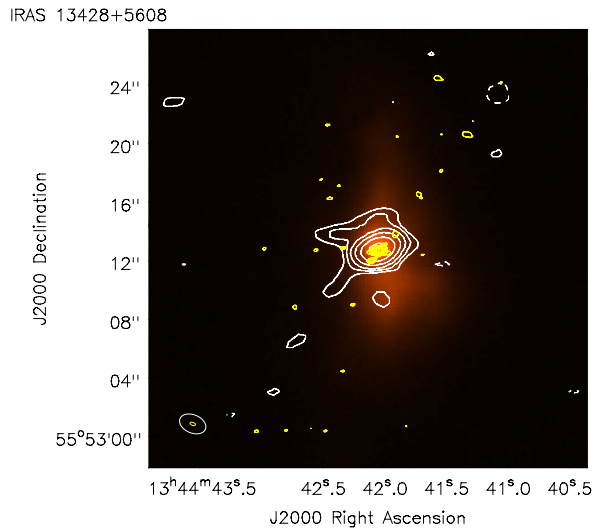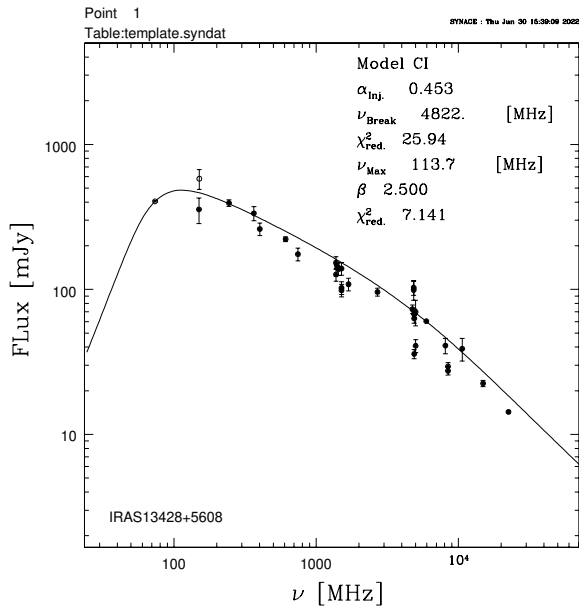
Figure 4.8: Radio Spectrum of IRAS 13428+5608 with their best fitting model is on the left panel. The vertical axis is the flux density in mJy, and the horizontal axis is the frequency in MHz in the log scale. 14.9 GHz VLA radio contours are plotted at $3\sigma[1, 1, 2, 4, 8, 16, 32, 64, 128]$ in white, 8.46 GHz VLA contours are plotted at $3\sigma[2, 4, 8, 16, 32, 64, 128]$ in yellow and overlaid on Pan-STARRS r-band optical image in the right panel.

Chapter 5

Discussions and Conclusions

5.1 Until now...

5.1.1 Spectral ages and Time scales of the evolution of radio galaxies

The spectral ages of 8 ULIRGs were calculated. The sources show young ages with an average of 3 million years, except for sources IRAS 10494+4424 and IRAS 12127-1412 which show possible spectral ages of up to 35 and 83 million years, respectively. This is because this source's high-resolution data are unavailable; the volume may be overestimated in this instance, resulting in high spectral age.

Hence, observing the sources at as many frequencies as possible is important. The high-frequency data will be essential to constrain the break frequency and the volume of the sources to calculate the spectral age of the source better. The low-frequency data will be necessary to constrain the turnover frequency, helping us relate the sources to GPS/CSS sources.

Our analysis of spectral ageing indicates that the sources are younger than the remnant or large extended radio sources, which are aged $10^7 - 10^8$ million years old [24]. Hence, the spectral ages are consistent with the hypothesis of ULIRGs being young radio sources.

The timescales that decide the evolution of ULIRGs into radio galaxies with kpc-sized jets are the galaxy merger timescales and the supermassive black hole coalescence timescales. The coales-

cence of supermassive black holes occurs on the timescale of $10^8 - 10^9$ years. The supermassive black holes may become active pre-coalescence, or post-coalescence [39]. The time taken by radio jets to extend to 100 kpc at the speed of $0.1c$, where c is the speed of light is $10^6 - 10^7$ years [24]. Since these time scales are much shorter than the time ULIRGs at $z \sim 0.1$ have to evolve (~ 1.3 Gyrs), there is no timescale issue for ULIRGs to evolve into radio galaxies.

5.1.2   GPS/CSS sources and ULIRGs

The turnover frequencies of the sample of ULIRGs are < 500 MHz except for IRAS 05156-3024, which does not show a turnover in the spectrum. So, ULIRGs' spectral profile is similar to that of CSS sources.

The sample size of the number of ULIRGs studied to find characteristics of GPS/CSS sources is not yet statistically significant. Hence, more ULIRGs need to be examined to understand their significance in the evolution of GPS/CSS sources into large radio galaxies.

5.1.3   Resolved sources

We have two resolved sources in our sample, IRAS 05189-2524 and IRAS 13428+5608. IRAS 05189-2524 shows a double-lobed structure at 8.49 GHz. It is a double nuclei system in optical, as discussed in Section 4.1. It is unclear from the overlay (See panel 2 in Figure 4.3) if the radio emission is extended emission from the individual nuclei or if one of the nuclei is an AGN with jets. IRAS 13428+5608 is a three nuclei system [39].

Optical spectrum studies are necessary to clarify the presence of two nuclei through the existence of double peaks in the spectrum from two AGNs. One needs to be careful, as double peaks in the spectrum can also occur due to a rotating nuclear disk in the system.

5.2   What's next?

Our goal is to gain a better understanding of the evolution of radio galaxies by studying more Ultra Luminous Infrared Galaxies (ULIRGs) and analyzing their radio spectrum. To achieve this,

we will observe both high and low radio frequencies. The Great Observatories All-sky Survey-Equatorial VLA Survey (GOALS-ES) [40] is a data set that includes radio data from 3-33 GHz, as well as data from other wavelengths, and it contains information about a large number of U/LIRGs. By using this data set, we can repeat the work done in this thesis and draw statistically significant conclusions about the evolution of ULIRGs.

Furthermore, we will expand our study to include other wavelengths, such as X-rays, which have a greater ability to penetrate dust than UV/optical light. Additionally, we will examine the optical spectra of the systems to identify any double-peaked structures that may be associated with the presence of double nuclei in the system.

To identify the presence and classification of Active Galactic Nuclei (AGNs) in the system, we will analyze the spatial variation of the spectral index and radio morphologies [41]. By correlating this information with infrared and optical line ratio diagnostics of AGN, we can gain a deeper understanding of the evolution of radio galaxies.

5.3   In summary...

- In this thesis, ULIRGs' radio energy distribution was studied. Three small extended radio emissions sources were seen: IRAS 11119+3257, IRASF 07599+6508, and IRAS 01569-2939. These emissions might originate from an outflow or a core-jet radio structure.

- These sources' radio powers at 1.4 GHz have been identified to be very near to the radio power that separates FRI and FRII sources at $\log P_{1.4\text{GHz}} = 25$.

- By utilising archival data, we analysed the radio spectra of all the sources. Except for IRAS 05156-3024, which does not show a turnover in the spectrum, we detected a low-frequency turnover in all the sources.

- The average spectral age was found to be approximately 3 million years.

- The radio spectrum, synchrotron age and morphology resemble GPS/CSS sources.

- We obtained resolved structures for two sources (IRAS 05189-2524, IRAS 13428+5608) at high frequencies.

Appendix A

Equipartition theory and Synchrotron Age

A.1 Derivation of radio luminosity for a radio source at redshift z

The radio flux density S_ν is related to frequency ν by

$$S_\nu \propto \nu^{-\alpha} \implies S_\nu = S_0 \left(\frac{\nu}{\nu_0} \right)^{-\alpha} \tag{A.1}$$

where

- α is the spectral index

- S_0 is the flux density at frequency ν_0

The k-corrected radio luminosity L_ν for a radio source at redshift z is given by [25],

$$L_\nu = 4\pi D_L^2 S_\nu (1+z)^{\alpha-1} \tag{A.2}$$

- D_L is the luminosity distance

- S_v is the radio flux density

The radio power at 1.4 GHz from Equation A.2 is then given by,

$$\log_{10}[P_{1.4GHz}] = \log_{10}\left[4\pi D_L^2 S_v (1+z)^{\alpha-1}\right] \tag{A.3}$$

The radio power between an upper and lower frequency limit can be obtained by integrating Equation A.2

$$L = \int_{v_l}^{v_u} L_v \, dv = \int_{v_l}^{v_u} 4\pi D_L^2 S_v (1+z)^{\alpha-1} \, dv$$

where v_l, v_u are lower and upper-frequency limits, respectively. Substituting Equation A.1

$$L = \int_{v_l}^{v_u} 4\pi D_L^2 S_0 \left(\frac{v}{v_0}\right)^{-\alpha} (1+z)^{\alpha-1} \, dv$$

$$= 4\pi D_L^2 (1+z)^{\alpha-1} S_0 v_0^{\alpha} \int_{v_l}^{v_u} v^{-\alpha} \, dv$$

$$= 4\pi D_L^2 (1+z)^{\alpha-1} S_0 v_0^{\alpha} \left.\frac{v^{-\alpha+1}}{-\alpha+1}\right|_{v_l}^{v_u}$$

$$L = 4\pi D_L^2 (1+z)^{\alpha-1} S_0 v_0^{\alpha} (v_u^{1-\alpha} - v_l^{1-\alpha})(1-\alpha)^{-1} \tag{A.4}$$

A.2 Deriving minimum magnetic field for equipartition condition

The minimum magnetic field within the source can be estimated in the following way [42]:

Let the electrons have power law distribution described by

$$N(E) = N_0 E^{-\gamma} \tag{A.5}$$

The luminosity between energies E_1 and E_2 is

$$L = -\int_{E_1}^{E_2} \frac{dE}{dt} N(E) \, dE \tag{A.6}$$

where $-dE/dt$ is the rate of loss of particle energy due to synchrotron radiation

$$-\frac{dE}{dt} = c_2 B^2 \sin^2 \theta E^2 \tag{A.7}$$

where

- $c_2 = \frac{2e^4}{3m^4 c^7} = 2.37 \times 10^{-3} \text{s}^3 \, \text{cm}^{-1} \, \text{g}^{-2}$ for electrons and positrons

- B is the magnetic field

- θ is the pitch angle of the electron

Substituting Equation A.7 and Equation A.5 in Equation A.6

$$L = \int_{E_1}^{E_2} c_2 B^2 \sin^2 \theta E^2 N_0 E^{-\gamma} \, dE$$

$$= N_0 c_2 B^2 \sin^2 \theta \int_{E_1}^{E_2} E^{-\gamma+2} \, dE$$

$$\implies N_0 = \frac{L}{c_2 B^2 \sin^2 \theta \int_{E_1}^{E_2} E^{-\gamma+2} \, dE} \tag{A.8}$$

The total energy of electrons is

$$E_e = \int_{E_1}^{E_2} E N(E) \, dE \tag{A.9}$$

Substituting Equation A.5 and Equation A.8 in Equation A.9

$$E_e = c_2^{-1} L (B \sin \theta)^{-2} \frac{\int_{E_1}^{E_2} E^{-\gamma+1} dE}{\int_{E_1}^{E_2} E^{-\gamma+2} dE}$$

$$= c_2^{-1} L (B \sin \theta)^{-2} \frac{\gamma - 3}{\gamma - 2} \frac{E_2^{-\gamma+2} - E_1^{-\gamma+2}}{E_2^{-\gamma+3} - E_1^{-\gamma+3}} \tag{A.10}$$

Since electrons radiate most of their energy in the neighbourhood of their critical frequencies ν_c, we can replace the energies E_1, E_2 with respective critical frequencies ν_1, ν_2

$$\nu_c = c_1 B \sin \theta E^2 \tag{A.11}$$

where $c_1 = \frac{3e}{4\pi m^3 c^5} = 6.27 \times 10^{18} \mathrm{s}^4 \, \mathrm{cm}^{-7/2} \, \mathrm{g}^{-5/2}$ for positrons and electrons

$$\implies \nu_1 = c_1 B \sin \theta E_1^2 \implies E_1 = \frac{\nu_1}{c_1 B \sin \theta} \tag{A.12}$$

$$\implies \nu_2 = c_1 B \sin \theta E_2^2 \implies E_2 = \frac{\nu_2}{c_1 B \sin \theta} \tag{A.13}$$

Using Equation A.12 and Equation A.13 in Equation A.10

$$E_e = c_2^{-1} c_1^{1/2} L (B \sin \theta)^{-3/2} \frac{\gamma - 3}{\gamma - 2} \frac{\nu_2^{(-\gamma+2)/2} - \nu_1^{(-\gamma+2)/2}}{\nu_2^{(-\gamma+3)/2} - \nu_1^{(-\gamma+3)}/2}$$

$$= c_2^{-1} c_1^{1/2} L (B \sin \theta)^{-3/2} \frac{2\alpha - 2}{2\alpha - 1} \frac{\nu_2^{(1-2\alpha)/2} - \nu_1^{(1-2\alpha)/2}}{\nu_2^{1-\alpha} - \nu_1^{1-\alpha}} \tag{A.14}$$

where $\alpha = -\frac{1-\gamma}{2}$ is the spectral index.

By defining

$$c_{12} = c_2^{-1} c_1^{1/2} \frac{2\alpha - 2}{2\alpha - 1} \frac{v_2^{(1-2\alpha)/2} - v_1^{(1-2\alpha)/2}}{v_2^{1-\alpha} - v_1^{1-\alpha}} \tag{A.15}$$

Equation A.14 can be rewritten as

$$E_e = c_{12} L (B \sin \theta)^{-3/2} \tag{A.16}$$

The total energy E_{total} within a radio source is

$$E_{total} = E_e + E_p + E_H \tag{A.17}$$

- E_p is the total energy of heavy particles

- E_H is the energy in the magnetic field

We will assume that the heavy particle energy is k times the electron energy, in which k depends on the mechanism of generation of relativistic electrons. It can range from $k \approx 1$ if the source of electrons is from the annihilation of matter and antimatter to $k \approx 2000$ for the induction-type mechanism. As the mechanism is unknown, it is generally assumed to be equal to 1.

$$E_p = k E_e \tag{A.18}$$

The magnetic energy within a source of volume V is

$$E_H = \frac{B^2}{8\pi} \phi V \tag{A.19}$$

where ϕ is the fraction of the volume of the source occupied by the magnetic field and relativistic particles.

Substituting Equation A.18 and Equation A.19 into Equation A.17

$$E_{total} = (1+k)\,c_{12}\,(B\sin\theta)^{-3/2}\,L + \frac{B^2\,\phi\,V}{8\pi}$$

The minimum magnetic field within the source is then,

$$\frac{\partial E_{total}}{\partial B} = -\frac{3}{2}(1+k)\,c_{12}\,\sin^{-3/2}\theta\,B^{-5/2}\,L + \frac{B\,\phi\,V}{4\pi} = 0$$

$$\implies \frac{B_{min}\,\phi\,V}{4\pi} = \frac{3}{2}(1+k)\,c_{12}\,\sin^{-3/2}\theta\,B^{-5/2}\,L$$

$$B_{min} = [6\pi\,(1+k)c_{12}\sin^{-3/2}\theta L(V\phi)^{-1}]^{2/7} \tag{A.20}$$

When the electrons have an isotropically distributed pitch angle $<\sin^2\theta> = 2/3$

As most of the ULIRGs show deviation from the power law spectrum, estimating the luminosity by numerically integrating the non-power law spectrum is preferred.

Equation A.11 can be rearranged to

$$E = \sqrt{\frac{\nu}{c_1 B \sin\theta}} \tag{A.21}$$

Using Equation A.21 and A.7 in Equation A.6 we get,

$$N(E)dE = \frac{c_1}{c_2 B\sin\theta}\frac{L_\nu}{\nu}d\nu \tag{A.22}$$

Using Equation A.22 in Equation A.9,

$$E_e = \frac{c_1^{1/2}}{c_2(B\sin\theta)^{1/2}}\int\frac{L_\nu}{\nu^{1/2}}d\nu \tag{A.23}$$

Continuing the equipartition argument just like above,

$$B_{min} = \left(\frac{c_1^{1/2}}{c_2} \frac{6\pi(1+k)}{V\phi(\sin\theta)^{3/2}} \int \frac{L_v}{v^{1/2}} dv \right)^{2/7} \tag{A.24}$$

As $L_v = 4\pi D_L^2 S_v$,

$$B_{min} = \left(\frac{24\pi^2 D_L^2 c_1^{1/2}(1+k)}{c_2 V\phi(\sin\theta)^{3/2}} \int \frac{S_v}{v^{1/2}} dv \right)^{2/7} \tag{A.25}$$

The values of v and S_v are in the emitter's frame. It can be converted to an observer's frame by,

$$B_{min} = (1+z) \left(\frac{24\pi^2 c_1^{1/2}(206265)^2}{c_2(\sin\theta)^{3/2}} \frac{(1+k)}{f_s\theta_x"\theta_y"s\phi} \int \frac{S_v}{v^{1/2}} dv \right)^{2/7} \tag{A.26}$$

as

- $V = \frac{f_s D_A^2 \theta_x"\theta_y"s}{(206265)^2}$

  - f_s is the shape factor for the volume emission region.
  - $\theta_x"$, $\theta_y"$ are the projected dimensions of the emission region in arcseconds
  - s is the depth of emission region

- $D_A = D_L/(1+z)^2$

- $S_v \to S_v(1+z)^{-1}$

- $v \to v(1+z)$

Appendix B

IRAS 11119+3257

B.1 Error Recognition - IRAS 11119+3257

We wanted to check if there is any extended emission in IRAS 11119+3257 at 1.4 GHz. VLA data of IRAS 11119+3257 was downloaded from the VLA archive and calibrated through a pipeline. Before continuing with imaging, it is critical to examine the data quality and calibration.

The common sources of issues in radio astronomy are:

- Non-ideal calibrators: The properties of the calibrators may have altered since the last time they were observed.

- Atmosphere: The atmosphere can change over time over the telescope and interfere with the signal through emission.

- Radio Frequency Interference (RFI): RFIs are man-made signals that are extremely powerful in comparison to the radio source of interest's emissions.

- Malfunctioning antennas and correlators

- Astronomer's errors

These errors can be categorised into:

- Time-based: Time-based issues are pop-up when the telescope is not quite yet on the source, there are misbehaving antennas, there is shadowing of antennas, RFIs etc. While plotting data with respect to time, it is suggested to average over an orthogonal axis (channel) to better visualize the possible issues.

- Frequency-based: Frequency-based issues include RFIs, correlator-related issues and spectral lines. While plotting data with respect to frequency, it is suggested to average over an orthogonal axis (time) to better visualize the possible issues.

- Baseline-based: These generally point out the presence of RFI or structure in our sources. It is suggested to average over time and channel while plotting with UV-distance.

- Algorithm choices: These generally include the parameters chosen for imaging, like the number of pixels across the beam, gridder and deconvolver choices etc.

Calibrator sources have known properties and hence help us identify problems.

In the visibility domain, we can look at the following situations to understand if our calibration is 'ideal':

- The amplitude of the bandpass changes smoothly with frequency, and the phases are close to zero.

- The amplitude of the gain calibrator should be stable across time, with phases close to zero, as it is a point source.

- The amplitude of the flux calibrator should be consistent with the expected value and may have structure if it is an extended structure.

In the image domain, we expect:

- There are no sidelobes or artefacts in the images.

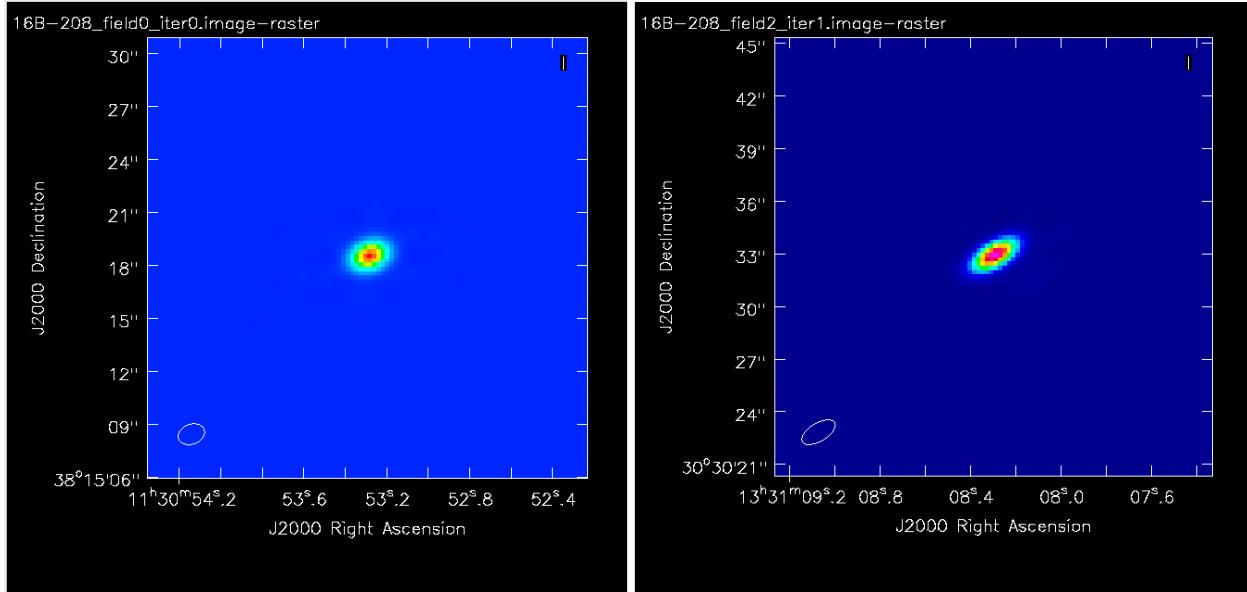- The calibrators' flux density is as expected (See Figure B.1).

Figure B.1: The images of the calibrators are plotted. The image of the flux calibrator on the right shows that it is a compact source. The flux we should get is 14.6 Jy [43]. The flux density obtained is 14.3 Jy. This is very close to the expected value. The image of the Phase Calibrator shows that it is a compact source. The flux density of the phase calibrator from `fluxscale` should be around 1.2 Jy. The flux extracted is very close to the value given by `fluxscale`.

Amplitude vs Time plots of point source calibrations must be constant, and their phases must be zero.

If Phase vs Time plots vary rapidly, usually due to hardware issues, we flag the bad antenna and make sure it is not used as the reference antenna to calculate phase solutions.

While plotting Amplitude vs UV-distance, the calibrators must have the right amplitudes. Extended sources have structure. Point sources must have constant amplitude with zero phases (See Figure B.2).

Point sources like the gain calibrators show a concise oval when Amplitude vs Phase is plotted (See Figure B.3).

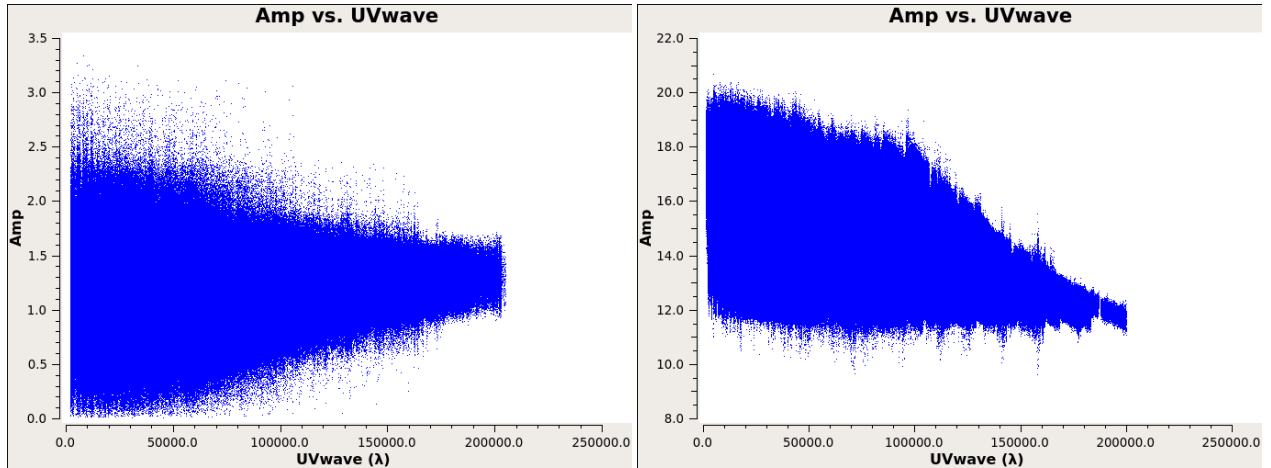The pipeline calibration is hence decent but can be improved.

Figure B.2: The Amplitude vs UV-Distance Plots for the calibrators are plotted. Both the Flux (on the right) and Gain calibrator (on the left) seem to show constant amplitude for shorter baselines like point sources and then show a steep drop in amplitude like extended sources at larger baselines

B.2 Calibrating IRAS 11119+3257

After flagging the data, the calibration was redone, and the solutions were plotted.

The calibration was applied to the dataset.

B.3 Imaging IRAS 11119+3257

We will now image IRAS 11119+3257. First, to determine the pixel size, we plot the amplitude vs. the UV-wave (UV distance in units of wavelength) plot. The maximum baseline D from the plot is 260000λ. The smallest angular size of the synthesized beam is hence $\lambda/D = 1/260000 = 0.8$ arcsec. Usually, 4 pixels are chosen to cover the size of the synthesized beam. Therefore each pixel measures $0.8/4 = 0.2$ arcsecs.

The image was made with different weights [44].

- Natural weighting: UV cells are weighted based on their RMS. The data visibility weights are gridded onto a UV-cell and added together. More visibility in a cell will thus raise the cell's weight, emphasising the shorter baselines. As a result of natural weighting, the surface brightness sensitivity improves, but the PSF increases, and the resolution suffers.
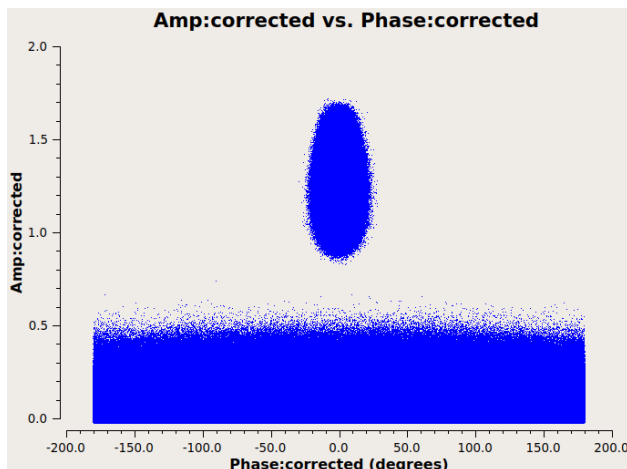
Figure B.3: Amplitude and Phase for the Gain calibrator in the MS for IRAS 11119+3257. The gain calibrator is a point source and is expected to have a confined oval centred at the known amplitude with a small spread in phase in the plot. We can see that while this is true, there is some 'bad data' that spreads below the oval. The data points were identified and flagged.

- Uniform weighing: The weights are gridded first, as in natural weighting, but each cell is rectified so that the weights are independent of the number of visibilities inside. The uniform weighting of the baselines represents UV-coverage better; in addition, sidelobes are suppressed more. When compared to natural weighing, uniform weighting typically favours longer baselines. As a result, the PSF is reduced, resulting in better image spatial resolution. However, the surface brightness sensitivity is diminished when compared to natural weighting.

- Briggs weighing: This method strikes a balance between natural and uniform weighting. The `robust` parameter can be used to regulate the transition.

	Briggs	Natural	Uniform
Beam Area	45.44	70.95	22.55
Flux Density (Jy)	0.1036	0.1004	0.1026

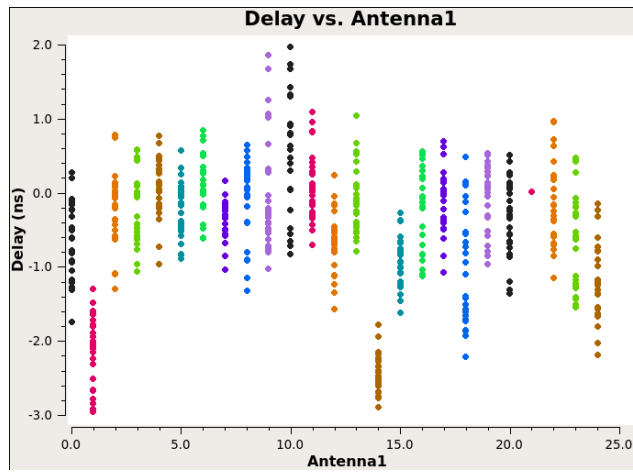Table B.1: Stats from different weights

Figure B.4: The delay solutions for IRAS 11119+3257 is plotted as a function of antennas. The delays are expected to be less than 4 ns for the upgraded VLA, which is seen in the plot
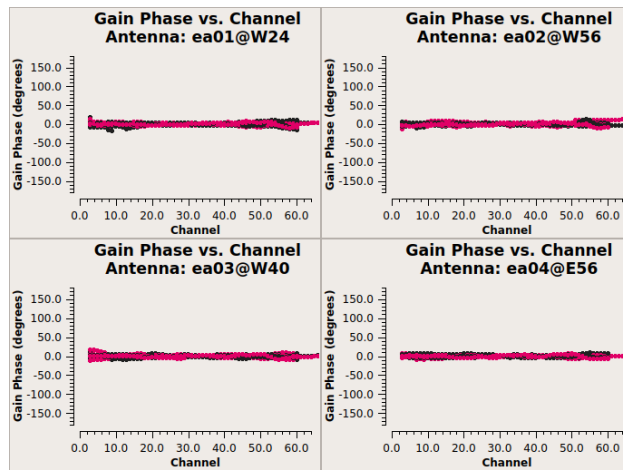

Figure B.5: The bandpass phases are plotted with channels on the x-axis for 4 baselines. We can see that the bandpass phases are relatively flat. The delay calibration removed the slopes.
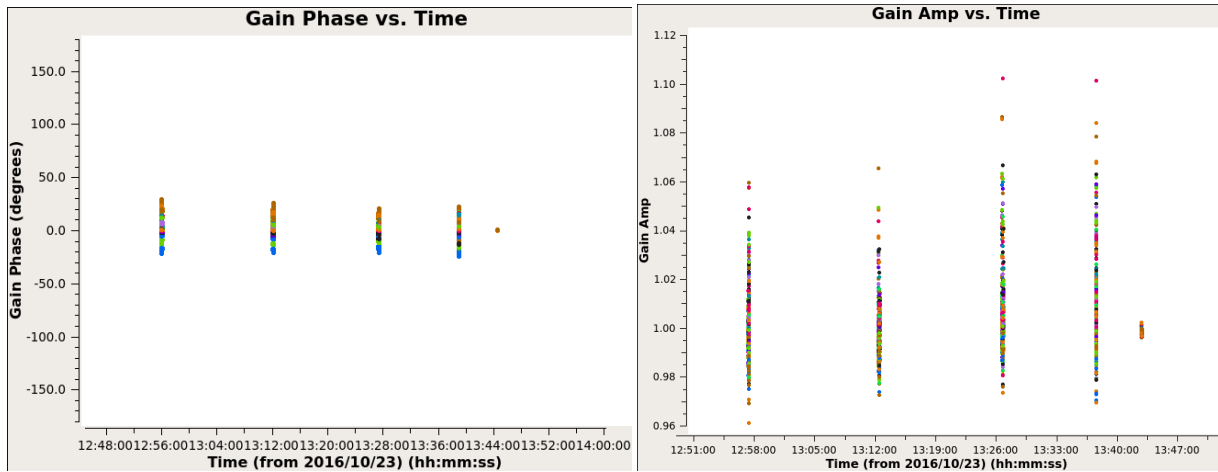
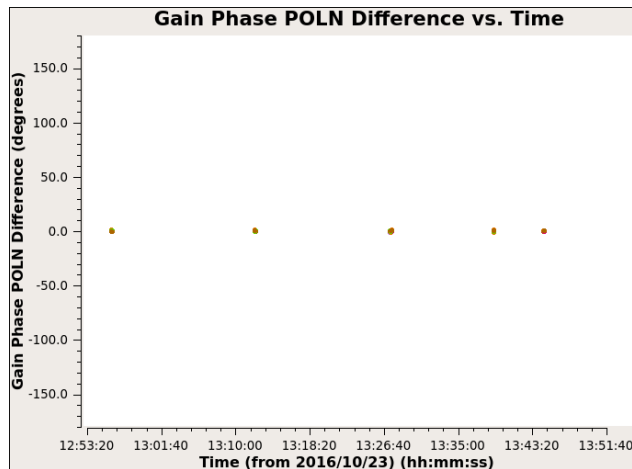Figure B.6: Gain Phase and Amplitude solutions plotted with time

Figure B.7: The plot is the ratio of gain phase solutions of the two polarisations for the chosen reference antenna. The phase stability of the reference antenna, i.e., to have a constant phase difference between the polarisations with time, can be tested. As the plot is relatively flat, we conclude that the chosen reference antenna is stable.
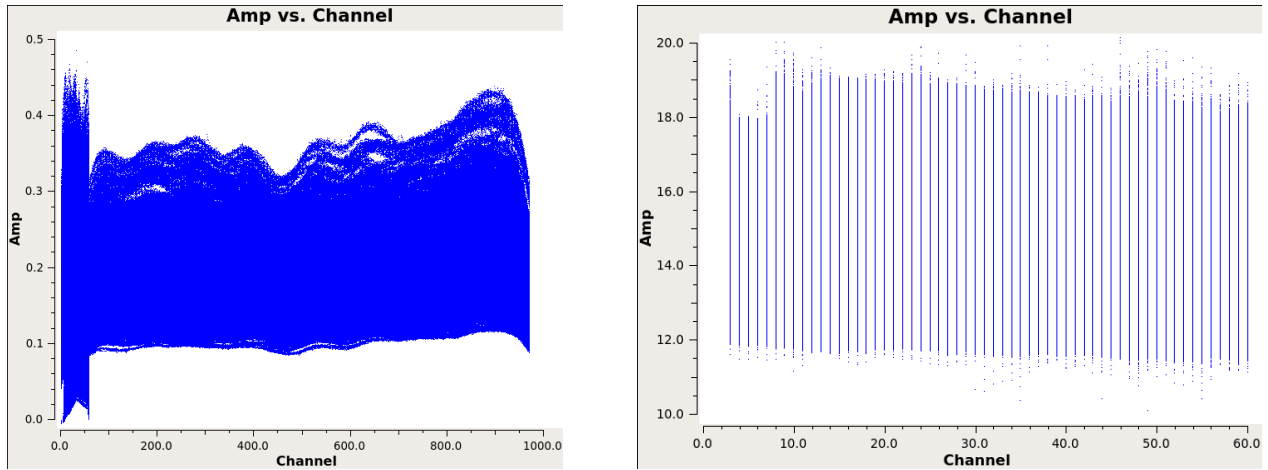
Figure B.8: Amplitude of the phase calibrator, before and after calibration. We can see that the effects of the bandpass are removed, and the flux calibration has fixed the amplitude of the calibrator.

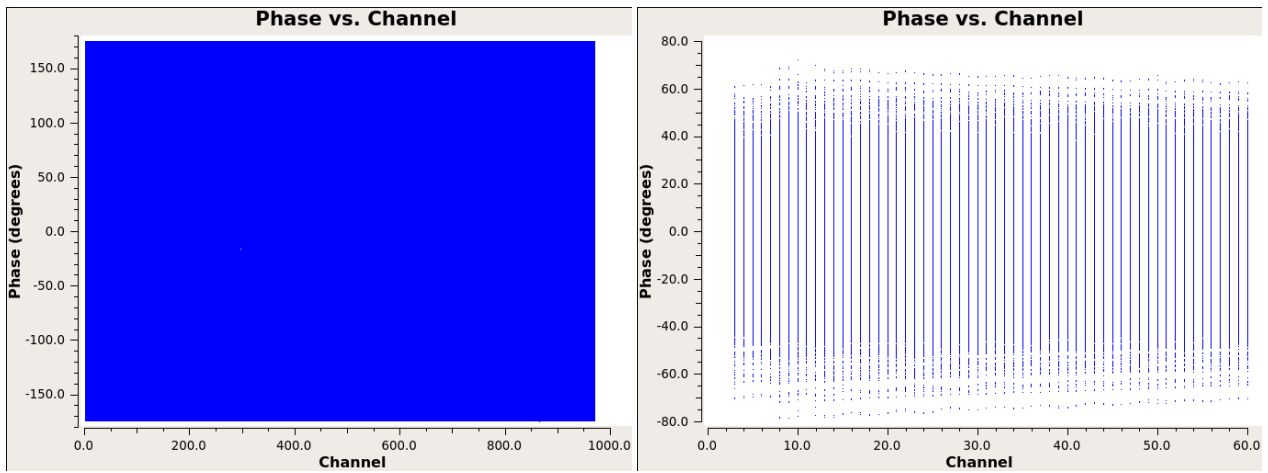Figure B.9: Phase of the phase calibrator, before and after calibration. The phase is now better constrained.

Briggs   **Natural**   **Uniform**
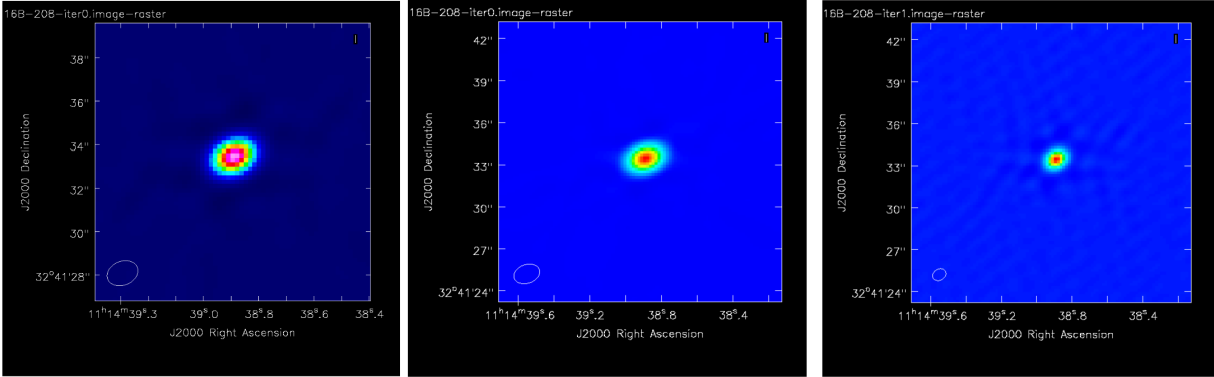

Figure B.10: Imaging of Source with different weights

Appendix C

PARAM Brahma and CASA

The parallelization approach adopted in `CASA` is the so-called "embarrassingly parallelization." This is frequently the case when there are little to no dependencies, needs for communication, or results between those parallel tasks [45].

All other parallelization is achieved by partitioning the Measurement Set (MS) using the task partition or at import using task `importasdm`. The resulting partitioned MS is called a "Multi-MS" or "MMS." Once `CASA` is started with `mpicasa` and the "Multi-MS" is created, there is no difference between running `CASA` in serial and parallel. The following calibration tasks are internally parallelized and will work on each Sub-MS in parallel: `flagdata, setjy, applycal, hanningsmooth, split,` etc.

Plots of the calibration table solutions for one of the VLA tutorials obtained from serial and parallel computation were compared. It was found that the solutions obtained were the same. But parallel processing using Multi-MS (MMS) in `CASA` is unverified and was suggested not to use.

The parallelization inside `tclean` does not need the MS to be partitioned into a Multi-MS. `tclean` is the `CASA` task with maximum gain from parallelization [46]. `tclean` on one of the VLA tutorials (MS file $\sim$ 6GB) in series and parallel on both the desktop and PARAM Brahma. The time taken for task `tclean` is noted down in the following table.

Parallelizing on the desktop has not significantly reduced the runtime. But the runtime is reduced to almost half the series processing value on PARAM. Running `tclean` in series on PARAM is

		Time taken for `tclean`
	Series	00:04:41
Desktop	Parallel 4 cores	00:04:09
	Parallel 8 cores	00:04:01
	Series	00:06:26
PARAM Brahma	Parallel 4 cores	00:04:54
	Parallel 8 cores	00:03:46

Table C.1: The time taken by `tclean` for the same dataset when ran on desktop and PARAM Brahma in series and parallel

more expensive than running it in series on the desktop.

As PARAM doesn't enable a Graphical User Interface, only non-interactive cleaning is possible. Hence, `tclean` on the supercomputer is suggested only after an initial `tclean` for self-calibration, where we will be more comfortable with `tclean` parameters and do not need interactive mode.

Bibliography

[1] E. P. Hubble. The classification of spiral nebulae. *Obs*, 50:276–281, 1927.

[2] D B Sanders and I F Mirabel. Luminous infrared galaxies. *Annu. Rev. Astron. Astrophys*, 34:749–92, 1996.

[3] C. J. Lonsdale, D. Farrah, and H. E. Smith. Ultraluminous infrared galaxies. pages 285–336.

[4] R. Genzel, L. J. Tacconi, D. Rigopoulou, D. Lutz, and M. Tecza. Ultraluminous infrared mergers: Elliptical galaxies in formation? *The Astrophysical Journal*, 563:527–545, 12 2001.

[5] Malcolm S. Longair. *High Energy Astrophysics*. 2011.

[6] J. J. Condon. Radio emission from normal galaxies. , 30:575–611, January 1992.

[7] L. D. Anderson, T. M. Bania, J. M. Jackson, D. P. Clemens, M. Heyer, R. Simon, R. Y. Shah, and J. M. Rathborne. THE MOLECULAR PROPERTIES OF GALACTIC h II REGIONS. *The Astrophysical Journal Supplement Series*, 181(1):255–271, mar 2009.

[8] D. B. Sanders, B. T. Soifer, J. H. Elias, B. F. Madore, K. Matthews, G. Neugebauer, and N. Z. Scoville. Ultraluminous Infrared Galaxies and the Origin of Quasars. , 325:74, February 1988.

[9] Carol J. Lonsdale, Harding E. Smith, and Colin J. Lonsdale. Ultraluminous Infrared Galaxies and the Radio-optical Correlation for Quasars. , 438:632, January 1995.

[10] Francesca Panessa, Ranieri D. Baldi, Ari Laor, Paolo Padovani, Ehud Behar, and Ian McHardy. The origin of radio emission from radio-quiet agn, 2019.

[11] T. Hayashi, Y. Hagiwara, and M. Imanishi. Radio properties of nearby ultraluminous infrared galaxies with luminous buried active galactic nuclei signatures. 2021.

[12] J. J. Condon, Z. P. Huang, Q. F. Yin, and T. X. Thuan. Compact Starbursts in Ultraluminous Infrared Galaxies. , 378:65, September 1991.

[13] M. S. Clemens, O. Vega, A. Bressan, G. L. Granato, L. Silva, and P. Panuzzo. Modeling the spectral energy distribution of ULIRGs. I. The radio spectra. , 477(1):95–104, January 2008.

[14] K. Rubinur, M. Das, P. Kharb, and M. Honey. A candidate dual agn in a double-peaked emission-line galaxy with precessing radio jets. *Monthly Notices of the Royal Astronomical Society*, 465:4772–4782, 3 2017.

[15] Christopher P. O'Dea. The Compact Steep-Spectrum and Gigahertz Peaked-Spectrum Radio Sources. , 110(747):493–532, May 1998.

[16] R. G. Carlberg. Quasar Evolution via Galaxy Mergers. , 350:505, February 1990.

[17] David S. De Young. The Evolution of Compact Steep Spectrum Sources. , 402:95, January 1993.

[18] D. J. Saikia. Compact steep-spectrum sources and the unified scheme. *Proceedings of the National Academy of Sciences of the United States of America*, 92(25):11417–11421, 1995.

[19] Stefi A. Baum, Esther L. Zirbel, and Christopher P. O'Dea. Toward understanding the fanaroff-riley dichotomy in radio source morphology and power. *ApJ*, 451:88, 9 1995.

[20] Fanaroff-riley classification.

[21] Ivan Marti-Vidal. Apsynsim: An interactive tool to learn interferometry, 2017.

[22] D.-C. Kim and D. B. Sanders. The iras 1 jy survey of ultraluminous infrared galaxies. i. the sample and luminosity function. *The Astrophysical Journal Supplement Series*, 119:41–58, 11 1998.

[23] M. Murgia, C. Fanti, R. Fanti, L. Gregorini, U. Klein, K. H. Mack, and M. Vigotti. Synchrotron spectra and ages of compact steep spectrum radio sources. , 345:769–777, May 1999.

[24] S. Nandi, M. Das, and K. S. Dwarakanath. Tracing the evolution of ultraluminous infrared galaxies into radio galaxies with low frequency radio observations. *Monthly Notices of the Royal Astronomical Society*, 503:5746–5762, 2 2021.

[25] E. Donoso, P. N. Best, and G. Kauffmann. Evolution of the radio-loud galaxy population. *Monthly Notices of the Royal Astronomical Society*, 392(2):617–629, jan 2009.

[26] C. Konar, M. Jamrozy, D. J. Saikia, and J. Machalski. A multifrequency study of giant radio sources - i. low-frequency giant metrewave radio telescope observations of selected sources. *Monthly Notices of the Royal Astronomical Society*, 383(2):525–538, dec 2007.

[27] W. A. Joye and E. Mandel. New Features of SAOImage DS9. In H. E. Payne, R. I. Jedrzejewski, and R. N. Hook, editors, *Astronomical Data Analysis Software and Systems XII*, volume 295 of *Astronomical Society of the Pacific Conference Series*, page 489, January 2003.

[28] J. P. McMullin, B. Waters, D. Schiebel, W. Young, and K. Golap. CASA Architecture and Applications. In R. A. Shaw, F. Hill, and D. J. Bell, editors, *Astronomical Data Analysis Software and Systems XVI*, volume 376 of *Astronomical Society of the Pacific Conference Series*, page 127, October 2007.

[29] H. van der Laan and G. C. Perola. Aspects of radio galaxy evolution. *AA*, 3:468, 1969.

[30] S. Veilleux, D.-C. Kim, and D. B. Sanders. Optical and near-infrared imaging of the iIRAS/i 1 jy sample of ultraluminous infrared galaxies. II. the analysis. *The Astrophysical Journal Supplement Series*, 143(2):315–376, dec 2002.

[31] D. L. Clements, W. J. Sutherland, R. G. McMahon, and W. Saunders. Optical imaging of ultraluminous IRAS galaxies: how many are mergers? *Monthly Notices of the Royal Astronomical Society*, 279(2):477–497, 03 1996.

[32] D.L. Clements, W. J. Sutherland, W. Saunders, G. P. Efstathiou, R. G. McMahon, S. Maddox, A. Lawrence, and M. Rowan-Robinson. A new large sample of ultraluminous IRAS galaxies. *Monthly Notices of the Royal Astronomical Society*, 279(2):459–476, 03 1996.

[33] Sylvain Veilleux, D. B. Sanders, and D. C. Kim. New Results from a Near-Infrared Search for Hidden Broad-Line Regions in Ultraluminous Infrared Galaxies. , 522(1):139–156, September 1999.

[34] Charlene Anne Heisler and J. Patricia Vader. Galaxies With Spectral Energy Distribution Peaking Near 60microns. II. Optical Broadband Properties. , 107:35, January 1994.

[35] Jason A. Surace, D. B. Sanders, William D. Vacca, Sylvain Veilleux, and J. M. Mazzarella. Hst/wfpc2 observations of warm ultraluminous infrared galaxies*. *The Astrophysical Journal*, 492(1):116, jan 1998.

[36] L. J. Tacconi, R. Genzel, D. Lutz, D. Rigopoulou, A. J. Baker, C. Iserlohe, and M. Tecza. Ultraluminous Infrared Galaxies: QSOs in Formation? , 580(1):73–87, November 2002.

[37] J. Rodríguez Zaurín, C. N. Tadhunter, and R. M. González Delgado. The properties of the stellar populations in ULIRGs - I. Sample, data and spectral synthesis modelling. , 400(3):1139–1180, December 2009.

[38] M. P. Véron-Cetty and P. Véron. A catalogue of quasars and active nuclei: 12th edition. , 455(2):773–777, August 2006.

[39] P. Kukreti, R. Morganti, M. Bondi, T. Oosterloo, C. Tadhunter, L. K. Morabito, E. A. K. Adams, B. Adebahr, W. J. G. de Blok, F. de Gasperin, A. Drabent, K. M. Hess, M. V. Ivashina, A. Kutkin, Á . M. Mika, L. C. Oostrum, T. W. Shimwell, J. M. van der Hulst, J. van Leeuwen, R. J. van Weeren, D. Vohl, and J. Ziemke. Seeing the forest and the trees: A radio investigation of the ULIRG mrk 273. *Astronomy &amp Astrophysics*, 664:A25, aug 2022.

[40] S. T. Linden, Y. Song, A. S. Evans, E. J. Murphy, L. Armus, L. Barcos-Muñoz, K. Larson, T. Díaz-Santos, G. C. Privon, J. Howell, J. A. Surace, V. Charmandaris, U. Vivian, A. M. Medling, J. Chu, and E. Momjian. A very large array survey of luminous extranuclear star-forming regions in luminous infrared galaxies in goals. *The Astrophysical Journal*, 881:70, 8 2019.

[41] E. Vardoulaki, V. Charmandaris, E. J. Murphy, T. Diaz-Santos, L. Armus, A. S. Evans, J. M. Mazzarella, G. C. Privon, S. Stierwalt, and L. Barcos-Muñoz. Radio continuum properties of luminous infrared galaxies. Identifying the presence of an AGN in the radio. , 574:A4, February 2015.

[42] Pacholczyk and A. G. Radio astrophysics. nonthermal processes in galactic and extragalactic sources. *ranp*, 1970.

[43] Calibrating the flux density scale — science website.

[44] Vla casa imaging-casa6.5.2 - casa guides.

[45] Parallel processing — casadocs documentation.

[46] Running casa in parallel.